# **Amora: Black-box Adversarial Morphing Attack**

Run Wang<sup>1</sup>, Felix Juefei-Xu<sup>2</sup>, Xiaofei Xie<sup>1</sup>, Lei Ma<sup>3</sup>, Yihao Huang<sup>4</sup>, Yang Liu<sup>1</sup>

<sup>1</sup>Nanyang Technological University, <sup>2</sup>Alibaba Group, <sup>3</sup>Kyushu University <sup>4</sup>East China Normal University

#### Abstract

Nowadays, digital facial content manipulation has become ubiquitous and realistic with the unprecedented success of generative adversarial networks (GANs) in image synthesis. Unfortunately, face recognition (FR) systems suffer from severe security concerns due to facial image manipulations. In this paper, we investigate and introduce a new type of adversarial attack to evade FR systems by manipulating facial content, called adversarial morphing attack (a.k.a. Amora). In contrast to adversarial noise attack that perturbs pixel intensity values by adding human-imperceptible noise, our proposed adversarial morphing attack is a semantic attack that perturbs pixels spatially in a coherent manner. To tackle the black-box attack problem, we have devised a simple yet effective learning pipeline to obtain a proprietary optical flow field for each attack. We have quantitatively and qualitatively demonstrated the effectiveness of our adversarial morphing attack at various levels of morphing intensity on two popular FR systems with smiling facial expression manipulations. Experimental results indicate that a novel black-box adversarial attack based on local deformation is possible, which is vastly different from additive noise based attacks. The findings of this work may pave a new research direction towards a more thorough understanding and investigation of image-based adversarial attacks and defenses.

## 1. Introduction

Human faces are important biometrics in identity recognition and access control such as security check, mobile payment, and attendance recording, *etc*. Thus, more and more face recognition systems are widely applied in various fields for improving the service qualities and securing crucial assets. In recent years, research has shown that current FR systems are vulnerable to various attacks (*e.g.*, presentation spoofing attack [40] and adversarial noise attack [2]), which bring severe security concerns to the FR systems deployed in security-sensitive applications like payment. In our work, we investigate that FR systems are also vulnerable to another new type of adversarial attack, called adversarial morphing attack, by perturbing pixels spatially in a coherent manner, instead of perturbing pixels by adding imperceptible noise like adversarial noise attack.

Figure 1 presents three different types of attacks to the FR systems, namely presentation spoofing attack, adversarial noise attack, and our proposed adversarial morphing attack. Presentation spoofing attack is a rather simple attack method by presenting a printed paper, wearing eyeglass, *etc*. In contrast to presentation spoofing attack without any pixels perturbation, adversarial noise attack perturbs pixels in images by adding imperceptible noise. Our proposed adversarial morphing attack is a non-additive approach that perturbs pixels spatially in a coherent manner, while adversarial noise attack adds imperceptible noise. Adversarial noise attack is also called adversarial example attack and studies demonstrated that deep neural networks are vulnerable to adversarial examples which are widely found in image [12], texts [10], audio [48], and even malware [13], *etc*. Compared with physical spoofing attack, adversarial attack manipulating pixels can be hardly detected and poses more severe security concerns than presentation spoofing attack.

Next, we discuss the attack model and present some basic requirements for adversarial attacks. In black-box adversarial attacks, we assume that the attacker can hardly obtain the knowledge of the objective model and can only attack the model with limited times by querying successful attack patterns. The ultimate goal of the attack is to evade the model by triggering erroneous output and reducing their performance in classification. The basic requirements of adversarial attacks are presented as follows.

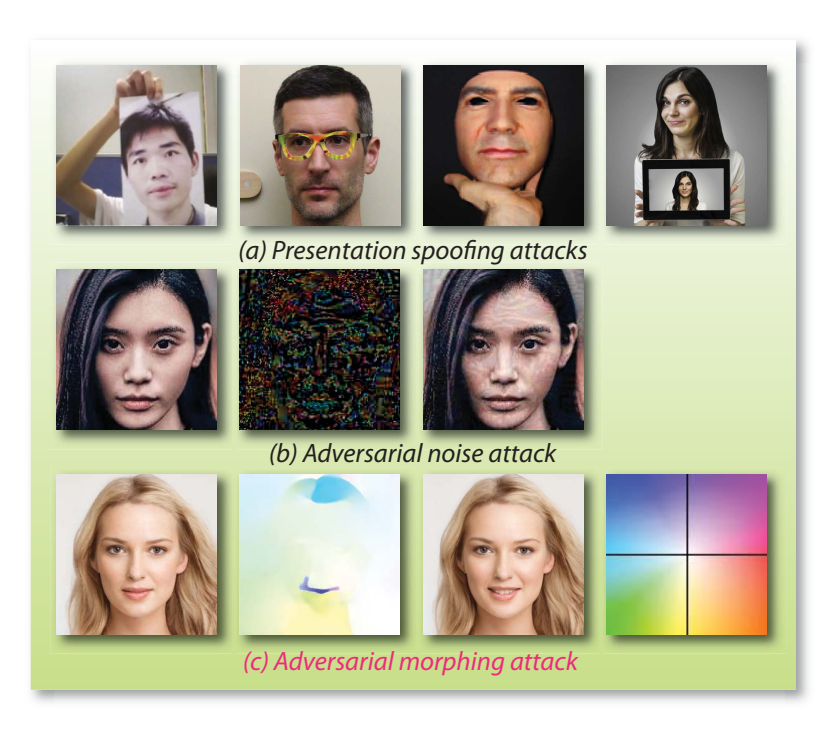


**Figure 1:** Three typical attacks to FR systems. (a) presentation spoofing attacks (*e.g.*, print attack [7], disguise attack [40], mask attack [25], and replay attack [3]), (b) adversarial noise attack [31, 7, 12], (c) proposed adversarial morphing attack.

- 1. The attack should be performed in a *black-box* manner. Most of the time, attackers can hardly obtain any knowledge of the model including model architecture, parameters, and training data, *etc*.
- 2. The attack should be *transferable*. The crafted examples that attack one target FR system successfully should have high attack success rate on other FR systems.
- 3. The attack should be *controllable*. Attackers can control the perturbations in generating adversarial faces and query the successful attack faces in limited times.
- 4. The crafted attack samples look *visually realistic* and *semantically sound* to humans. It would be better without any obvious artifacts in the generated adversarial faces.

Our adversarial morphing attack satisfies all of the above four requirements. We can effectively attack FR systems without obtaining any knowledge of the model in a total black-box scenario and easily transfer to compromising other FR systems. In attacking FR systems, the adversarial faces are morphed with a learned proprietary morphing field and look visually realistic to the original faces. Figure 2 illustrates how to morph a face into an adversarial face with proprietary morphing field to tackle the black-box attack problem. We can also control the intensity of morphing fields to achieve a controllable attack.

Specifically, we first collect numerous frontal and near-frontal faces to attack FR systems. The successful queries lead to perpetrating faces and flow field pairs, which are used for learning the universal morphing field bases. Then, for any given face during the attack, we assign a proprietary morphing field in each individual attack. The main contributions of our work are summarized as follows.

- In this paper, we introduce a novel type of black-box adversarial attack, namely the black-box adversarial morphing attack, that morphs facial images with learned proprietary morphing field to generate visually realistic faces that are misclassified by two popular FR systems.
- We devise a simple yet effective method based on PCA to learn universal morphing field bases and proprietary morphing fields for generating adversarial faces to evade the FR systems.
- We have demonstrated the effectiveness of our adversarial morphing attack on two popular FR systems with smiling facial expression manipulations without obtaining any knowledge of the FR systems.

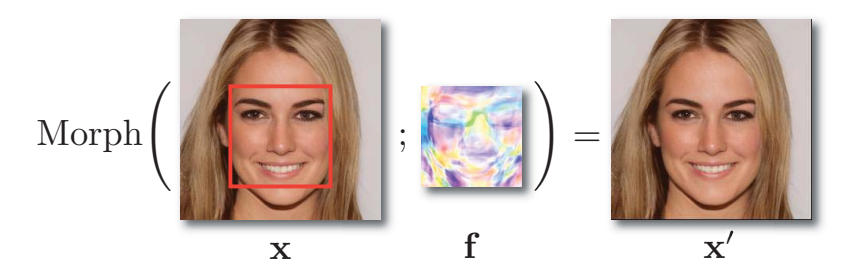


Figure 2: Adversarial morphing attack with proprietary morphing field. The change is very subtle, and x and x' are indeed different.

• Our research findings hint a new research field towards specification-based adversarial attacks and defenses by transforming images in a coherent and natural way, as opposed to adding incoherent noises like adversarial noise attack.

The remainder of our paper is organized as follows. Section 2 discusses the related work. Section 3 presents our proposed black-box adversarial morphing attack in detail. We show the experimental results and demonstrate the effectiveness of our proposed approach in attacking FR systems in Section 4. Finally, Section 5 concludes this paper and discusses future research directions.

#### 2. Related Work

#### 2.1. Adversarial Noise Attacks

The FR systems we will be dealing with in this work are all deep learning based ones. It has been demonstrated that, in spite of having achieved very high testing accuracy, deep neural networks are vulnerable to adversarial attacks [2].

White-box. White-box adversarial attacks require the full knowledge of the deep neural networks. A lot of adversarial attack techniques [12, 36, 5, 32] have been proposed. These techniques could be applied to attack the face recognition system. Specifically, the fast gradient sign method (FGSM) [11] generates the adversarial examples by performing one step gradient calculation, *i.e.*, adding the sign of gradient of the cost function to the input. Jacobian-based saliency map attack (JSMA) [36] computes the Jacobian matrix which identifies the impact of the input features on the final output, *i.e.*, which pixel has the most significant influence on the change of the output. C&W attack [5] is then proposed to generate adversarial attacks by solving the optimization problem whose basic idea of the objective function is to minimize the perturbation such that the output is changed. DeepFool [32] estimates the closest distance between the input and the decision boundary. Based on this, the minimal perturbation is calculated for adversarial examples.

**Black-box.** In a black-box attack setting, the attackers have no way to access model's parameters or structure and what they can utilize are only input-output pairs. Current techniques which are applied to generate adversarial samples in a black-box setting mainly rely on transferability, gradient estimation, and heuristic algorithms. Papernot *et al.* [35] first exploited the transferability property of adversarial samples to perform a black-box attack. They trained a substitute model based on the input-output relationships of the original model and crafted adversarial samples for the substituted model in a white-box manner. Narodytska *et al.* [33] proposed a local-search method to approximate the network gradients, which was then used to select a small fraction of pixels to perturb. Chen *et al.* [6] utilized the prediction score to estimate the gradients of target model. They applied zeroth-order optimization and stochastic coordinate descent along with various tricks to decrease sample complexity and improve its efficiency. Ilyas *et al.* [15] adopted natural evolutionary strategies to sample the model's output based on queries around the input and estimate gradient of the model on the input. In addition, noise-based attacks (white/black) may not be realistic, especially in face recognition domain. Differently, our morphing based method can generate a more realistic face which simulates diverse face reactions.

**Robustness.** There are also some techniques proposed for testing the robustness of the model against adversarial examples [49]. DeepXplore [37] proposed the neuron coverage criteria, based which the testing technique is proposed to test multiple deep neural networks (DNNs) as cross-referencing oracles. DeepGauge [29] then proposed a set of more fine-grained testing criteria, such as *k*-multisection Neuron Coverage, Neuron Boundary Coverage and *etc*. Based on the criteria, a general coverage-guided fuzzing technique, DeepHunter [46], is proposed to test the DNN by maximizing the coverage. In [28], the combinatorial testing criteria are proposed. The surprise metrics [24] are proposed to measure the surprise adequacy of the test set. DeepStellar [9] proposes a set of metrics for RNN testing based on an abstraction of the model. Then the coverage-guided testing technique is developed for testing RNN (*e.g.*, automatic speech recognition). TensorFuzz [34] is another fuzzing

framework based on the nearest neighbor metric. In addition, DeepMutation [30] is proposed to evaluate the quality and robustness of the data set and DiffChaser [47] detects the compatibility issues during the model deployment phase.

## 2.2. Adversarial Attacks on FR Systems

Sharif *et al.* [40] developed a method to generate attacks, which are realized through printing a pair of eyeglass frames and fool the face recognition system. Different from the noise-based approach, they adopt the optimization to calculate the perturbation on some restricted pixels (on the glasses frames) and they can be modified by a large amount. Similarly, Bose *et al.* [4] also generate adversarial attacks by solving the optimization constraints based on a generator network. These techniques are white-box attack, which is unrealistic in real-world applications. Additionally, some GAN-based attacking techniques have been proposed. Song *et al.* [41] proposed a GAN, which adds a conditional variational autoencoder and attention modules, for generating fake faces [42]. Deb *et al.* [7] proposed AdvFaces that learns to generate minimal perturbations in the salient facial regions via GAN. Dong *et al.* [8] adopted an evolutionary optimization method for generating adversarial samples which is a black-box method. The performance is improved by modeling the local geometry of search directions and reducing the search space. However, they still require many queries. So far there still lacks a work on black-box FR system attack based on pixel morphing that is fully addressed in this work.

#### 2.3. Non-additive Adversarial Attacks

The non-additive adversarial attacks have started to gain more traction in the research community. The work of [45] and [1] are the two prior methods that deal with white-box adversarial deformation attacks. In [45], the authors use a second order solver (L-BFGS) to find the deformation vector field, while in [1], a first-order method is formulated to efficiently solve such an optimization. Our method, in contrast, deals with a black-box setting where we cannot have access to the classifier parameters. Therefore, we need to devise a new method to facilitate such an adversarial morphing attack. Wasserstein adversarial attack [44] is also a non-additive attack under the white-box setting that is focused on norm-bounded perturbations based on the Wasserstein distance. The attack covers standard image manipulation such as scaling, rotation, translation, and distortion while our method is able to obtain semantically consistent proprietary morphing field even under a black-box setting. The defense against Wasserstein adversarial attack is also proposed [26]. In this work, we use optical flow as a way to realize facial image morphing and to carry out black-box attacks on the FR systems. It is worth noting that the proposed attack is not on the optical flow estimation step (see [38]), but rather on the FR classifier.

## 3. Proposed Method

Here, we first briefly review the adversarial noise attack and then present an overview of our adversarial morphing attack. Next, we detail the proposed adversarial morphing attack method to learn universal morphing field bases and obtain a proprietary morphing field for each individual attack.

#### 3.1. Brief Review of Adversarial Noise Attack

In the context of image (gray-scale, RGB, or higher-dimensional) classification problems, let  $\mathcal{C}$  be a classifier (shallow or deep) that maps the input image  $\mathbf{x} \in \mathbb{R}^N$  to a set of discrete and finite categories  $\mathcal{L} = \{1, 2, \dots, L\}$ . For simplicity,  $\mathbf{x}$  is a vectorized single-channel (gray-scale) image with N pixels in total. Adversarial noise perturbation attack aims to find a noise or error vector  $\mathbf{e} \in \mathbb{R}^N$  that is small in  $\ell_p$ -norm, i.e., imperceptible, such that when added to the input image can cause erroneous classifier output:

$$C(\mathbf{x} + \mathbf{e}) \neq C(\mathbf{x})$$
 and  $\|\mathbf{e}\|_p$  is small (1)

where  $\|\mathbf{e}\|_p = \left(\sum_i^N |\mathbf{e}_i|^p\right)^{1/p}$  for  $1 \leq p < \infty$  and when  $p = \infty$ ,  $\|\mathbf{e}\|_p$  is defined as  $\|\mathbf{e}\|_\infty = \max_{i=1,\dots,N} |\mathbf{e}_i|$ . The search for  $\mathbf{e}$  under white-box attack scenario is usually done by back-propagating classifier errors all the way to the noise vector  $\mathbf{e}$ . See Section 2 for a few popular algorithms. Let  $\mathbf{x}' \in \mathbb{R}^N$  be a adversarial noise-perturbed counterpart of  $\mathbf{x}$ , the image modification procedure can be summarized as:

$$\mathbf{x}' = \operatorname{Perturb}(\mathbf{x}; \mathbf{e}) = \mathbf{x} + \mathbf{e}$$
 (2)

Whereas, in this work, we are seeking a non-additive image modification method (spatial perturbation of pixels c.f. pixel value perturbation) with the aid of optical flow field:

$$\mathbf{x}' = \mathrm{Morph}(\mathbf{x}; \mathbf{f}^h, \mathbf{f}^v) \tag{3}$$

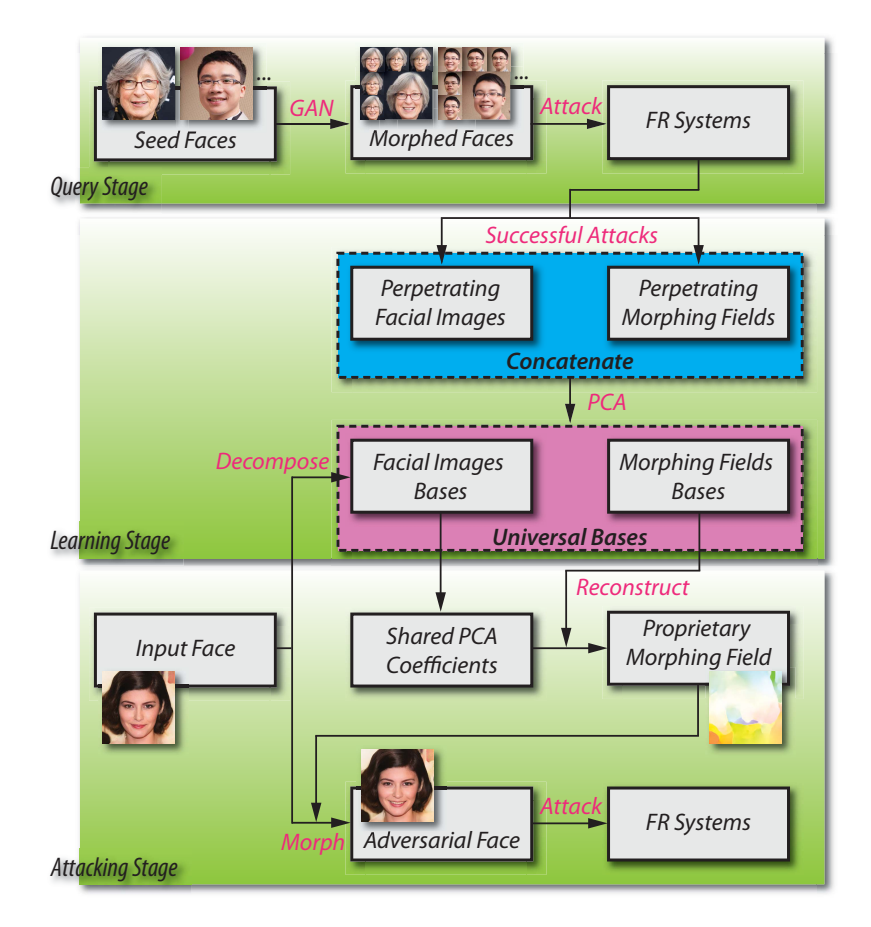


Figure 3: Overview of the proposed black-box adversarial morphing attack.

where  $\mathbf{f}^h \in \mathbb{R}^N$  and  $\mathbf{f}^v \in \mathbb{R}^N$  are the horizontal and vertical flow field respectively, and the concatenated whole field can be expressed as  $\mathbf{f}$ . The actual  $\mathrm{Morph}(\cdot)$  function works on 2D images, so there is an implicit step to map the vectorized image and flow fields back to 2D. Modifying images according to Equation (3) and causing classifier to output erroneously is what we call the *adversarial morphing attack*.

## 3.2. Overview of Adversarial Morphing Attack

Under the black-box adversarial morphing attack settings, the attackers do not have access to the model parameters (*i.e.*, deep learning based classifier), and thus obtaining the morphing field unique to each attack image by back-propagating the classifier errors through the network parameters is not feasible. In order to obtain proprietary morphing field, we propose to learn a set of universal morphing field bases, and through which, the proprietary morphing field can be reconstructed for each individual attack image. In the next two subsections, we will detail the learning procedure of the universal morphing field bases as well as how to assign a proprietary morphing field.

Figure 3 outlines the framework of our adversarial morphing attack to learn universal morphing field bases and obtain a proprietary morphing field for each individual attack image. It contains three essential stages: (1) query stage, (2) learning stage, and (3) attacking stage. In the query stage, we collect a set of seed faces and generate morphed faces with GAN to attack the FR systems. Then, in the learning stage, the successful attacks lead to the collection of perpetrating facial images as well as the morphing field, and from which we will learn the universal morphing field bases using principal components analysis (PCA) [43] by concatenating the perpetrating facial images and corresponding perpetrating morphing fields. Finally, in the attacking stage, we obtain a proprietary morphing field for an input face to morph it adversarially for attacking the FR systems.

#### 3.3. Learning Universal Morphing Field Bases

In preparing the training images to learn universal morphing field bases, we first collect numerous frontal and near-frontal faces to generate images with consecutive subtle facial expression change. Specifically, we leverage the power of GAN in

digital image manipulation to create a large amount of smiling facial images for each seed face. These morphed smiling facial images are smiled in a controllable way while ensuring other parts relatively unchanged. The consecutive set of smiling faces allows us to accurately capture the morphing field of smiling with optical flow which represents the motion of the pixels between two images. Details are shown in Section 4.

Once we have obtained a large number of (image, morphing field) pairs:  $(\mathbf{x}_i, \mathbf{f}_i)$  whose resulting morphed images  $\mathbf{x}_i'$  are successful in attacking the model, we can capitalize on the fact that there exists a correlation between the image  $\mathbf{x}_i$  and the 'perpetrating' morphing field  $\mathbf{f}_i$ . By stacking the corresponding counterparts as part of the same data point, we are implicitly enforcing a one-to-one mapping between the two domains (*i.e.*, image and morphing field), as practiced in [17, 18, 16, 20, 21, 19]. Once such a mapping is established between  $\mathbf{x}_i$ s and  $\mathbf{f}_i$ s through shallow or deep learning methods, we can potentially generate or reconstruct a proprietary 'perpetrating' morphing field for any image of interest. In this work, we use PCA, a simple yet effective method, to learn the universal morphing field bases. The training data matrix  $\mathbf{X} \in \mathbb{R}^{3N \times M}$  contains concatenated mean-subtracted image and flow field pairs in its columns, with a total of M instances:

$$\mathbf{X} = \begin{bmatrix} \mathbf{\Lambda}_x(\mathbf{x}_1 - \boldsymbol{\mu}_x), & \dots, & \mathbf{\Lambda}_x(\mathbf{x}_i - \boldsymbol{\mu}_x), & \dots \\ \mathbf{\Lambda}_h(\mathbf{f}_1^h - \boldsymbol{\mu}_h), & \dots, & \mathbf{\Lambda}_h(\mathbf{f}_i^h - \boldsymbol{\mu}_h), & \dots \\ \mathbf{\Lambda}_v(\mathbf{f}_1^v - \boldsymbol{\mu}_v), & \dots, & \mathbf{\Lambda}_v(\mathbf{f}_i^v - \boldsymbol{\mu}_v), & \dots \end{bmatrix}$$
(4)

where  $\Lambda_x \in \mathbb{R}^{N \times N}$ ,  $\Lambda_h \in \mathbb{R}^{N \times N}$ , and  $\Lambda_v \in \mathbb{R}^{N \times N}$  are diagonal dimensionality weighting matrices for the image, the two flow fields respectively. By setting certain diagonal elements to 0 in  $\Lambda_x$ ,  $\Lambda_h$ , and  $\Lambda_v$ , we can arbitrarily select the region of interest (ROI) in the optimization. In this work, the ROI is tight crop on the face region as shown in Figure 2 to ignore image deformations outside the face region that may contribute to the successful attacks. However, it might be interesting to explore that in a future work. The bases  $\mathbf{w}_i \in \mathbb{R}^{3N}$  can be obtained with the following optimization:

$$J(\mathbf{w}) = \underset{\|\mathbf{w}\|=1}{\arg\max} \left\{ \mathbf{w}^{\top} \mathbf{X} \mathbf{X}^{\top} \mathbf{w} \right\}$$
 (5)

$$= \underset{\|\mathbf{w}\|=1}{\arg\max} \left\{ \frac{\mathbf{w}^{\top} \mathbf{X} \mathbf{X}^{\top} \mathbf{w}}{\mathbf{w}^{\top} \mathbf{w}} \right\}$$
 (6)

$$= \arg\max_{\|\mathbf{w}\|=1} \left\{ \frac{\mathbf{w}^{\top} \mathbf{S}_{1} \mathbf{w}}{\mathbf{w}^{\top} \mathbf{S}_{2} \mathbf{w}} \right\}$$
 (7)

where  $\mathbf{S}_1 = \mathbf{X}\mathbf{X}^{\top}$  is the covariance matrix with  $\mathbf{X}$  being mean-subtracted, and  $\mathbf{S}_2 = \mathbf{I}$ . The objective function translates to a generalized Rayleigh quotient and the maximizer  $\mathbf{w}$  can be found by solving the eigen-decomposition of  $\mathbf{S}_2^{-1}\mathbf{S}_1$  which is  $\mathrm{eig}(\mathbf{S}_1)$ .

#### 3.4. Assigning Proprietary Morphing Field

For simplicity, let us assume  $\Lambda_x = \Lambda_h = \Lambda_v = \mathbf{I}$ . The leaned universal bases (principal components) can be broken down to an image portion  $\mathbf{w}_x \in \mathbb{R}^N$ , as well as morphing fields portions  $\mathbf{w}_h \in \mathbb{R}^N$  and  $\mathbf{w}_v \in \mathbb{R}^N$ . When an potential attack image  $\mathbf{y} \in \mathbb{R}^N$  comes in, we can decompose it with the top-K, (K < N) image portion bases  $(\mathbf{W}_x \in \mathbb{R}^{N \times K})$  and obtain the PCA projection coefficient vector  $\boldsymbol{\alpha} \in \mathbb{R}^K$ :

$$\boldsymbol{\alpha} = (\mathbf{W}_x^{\top} \mathbf{W}_x)^{-1} \mathbf{W}_x^{\top} \mathbf{y} \tag{8}$$

By forcing consistent PCA representations during training for both image and flow field, the mapping between the two is implicitly learned. Therefore, we can obtain the proprietary flow field  $\mathbf{f}_y \in \mathbb{R}^{2N}$  by reconstructing using the shared coefficients  $\alpha$  and the flow field portion  $\mathbf{W}_f = [\mathbf{W}_h; \mathbf{W}_v] \in \mathbb{R}^{2N \times K}$  of the bases:  $\mathbf{f}_y = \mathbf{W}_f \alpha$ .

Examples of proprietary morphing fields are shown in Figure 4. The first row is originally given faces and below is their proprietary morphing filed learned by our proposed approach.

#### 4. Experiments

In this section, we present the experimental results to demonstrate the effectiveness of our proposed adversarial morphing attack in evading close-set and open-set face recognition systems. We quantitatively and qualitatively evaluate our adversarial morphing attack on two popular FR systems under total black-box scenario. We also demonstrate the transferability of our adversarial morphing attack by investigating whether one adversarial face can be transferred to different FR systems. Additionally, we build two baselines to evaluate whether our learned proprietary morphing field could be served as guidance in morphing facial images.



Figure 4: Examples of proprietary morphing fields. The first row is the facial images, the second row is the tight cropped faces' corresponding proprietary optical flow.

## 4.1. Experimental Settings

**Target FR systems.** We study two popular FR systems, including VGG-Face<sup>1</sup> with VGG16 and ResNet50 as their architecture respectively. In testing, facial images are morphed by the learned proprietary optical flow field. Then, different intensity level optical flows are calculated to query the successful attack morphing fields. Finally, we use these morphing fields to evaluate the transferability of our attack.

**Dataset.** We conduct experiments on the CelebFaces Attributes Dataset (CelebA) [27] and CelebA-HQ [22].

- *CelebA* contains more than 202,599 face images and 10,177 identities. In training FR systems VGG-Face (VGG16) and VGG-Face (ResNet50) to evaluate the robustness of them in evading our generated morphing facial images, we select 2K and 1K identities from the *CelebA* dataset, respectively.
- CelebA-HQ<sup>2</sup> is a high-quality version of the CelebA dataset with more than 30K facial images in 1024x1024 resolution published by NVIDIA. We use this high quality facial images to generate smiling faces with StyleGAN [23] to attack FR systems.

**Evaluation metrics.** In attacking FR systems, the morphed facial images should be imperceptible to human eyes and is an adversarial face to FR systems which leads misclassification. Thus, we need to measure the similarity between the morphed and the original facial images to evaluate the performance of our attack method. We also report the mean attack success rate as well as the intensity of morphing fields. Specifically, we employ *Euclidean* distance ( $\ell_2$ -norm) and  $\ell_\infty$ -norm as metrics to measure the intensity of morphing fields. Additionally, we adopt SSIM and normalized cosine distance (NCS) as metrics to measure the perceptual similarity between original faces and morphed adversarial faces.

**Implementation details.** Our numerous smiling faces are morphed by StyleGAN and their optical flows are generated with FlowNet2 [14].

- StyleGAN Encoder<sup>3</sup> creates smiling faces by controlling the degree of smiling in a fine-grained way, which allows us to capture subtle smiling variations with optical flows.
- FlowNet2 [39] estimates optical flow between two consecutive images in a learning way. In our work, we use FlowNet2 to generate optical flows of facial images which attack the FR systems successfully.

All of our experiments are performed on a server running Ubuntu 16.04 system on an 18-core 2.30 GHz Xeon CPU with 200 GB RAM and an NVIDIA Tesla M40 GPU with 24 GB memory.

#### 4.2. Experimental Results

In this section, we report the experimental results on the *CelebA* dataset. Specifically, we mainly study the following research questions: 1) the effectiveness of the learned proprietary morphing fields in attacking FR systems, 2) the relation between the attack success rate and intensity of morphing fields, 3) the relation between the attack success rate and intensity

<sup>&</sup>lt;sup>1</sup>https://github.com/rcmalli/keras-vggface

<sup>&</sup>lt;sup>2</sup>https://github.com/tkarras/progressive\_growing\_of\_gans

<sup>&</sup>lt;sup>3</sup>https://github.com/Puzer/stylegan-encoder

	Seed Face	CelebA-HQ	CelebA
Identity	182	6,217	10,177
Facial image	18,200	30,000	202,599

Table 1: Identity and facial images of our collected dataset in the query stage, CelebA-HO, and CelebA.

	Attac	king	Traiı	ning
	Identity	Image	Identity	Image
VGG-Face (VGG16)	120	1,141	2,000	42,256
VGG-Face (ResNet50)	120	1,159	1,000	21,152

Table 2: Identities and facial images for attacking and training the two popular FR systems.

	VGG-Face (VGG16)	VGG-Face (ResNet50)
Identity	153	148
Morphing field	9,621	10,536

Table 3: Pair of facial image and morphing fields successfully attack FR systems in the query stage.

of morphed adversarial faces, 4) the transferabilities of our adversarial morphing attack and 5) the capabilities in attacking open-set face recognition systems.

**Data preparation.** In our experiment, we first collect 182 identities with frontal-face or near frontal-face from *CelebA-HQ* as seed faces to generate morphed smiling faces with StyleGAN. Table 1 presents the number of identities and facial images in our training dataset, *CelebA-HQ* and *CelebA*. In attacking the FR systems, we randomly select 120 identities including more than 1,000 facial images and morph them with proprietary morphing field to evaluate the robustness of FR systems to our adversarial morphing attack. Table 2 presents a detailed number of identities and facial images in attacking two popular FR systems.

To obtain successfully attacked perpetrating facial images and the pairing morphing fields, we need to attack some FR systems in the query stage. Table 2 presents the number of identities and their corresponding facial images in training the two popular FR systems (*e.g.*, VGG-Face (VGG16), VGG-Face (ResNet50)).

Collecting successful attack morphing fields. In our query stage, we generate numerous morphed facial images to attack FR systems to obtain successful attack perpetrating facial images and perpetrating morphing filed pairs for learning universal morphing field bases. Table 3 presents us the detailed statistical data of the successful attack pairs. More than 153 and 148 identities from 182 seed faces and nearly 10,000 facial images are successful attack the two popular FR systems. In order to obtain large numbers of facial image and morphing field pairs to learn a representative universal morphing field bases, we apply the following strategies to determine a successful attack. 1) causing erroneous output, which directly misclassifies the identity; 2) significant reducing the performance of FR systems, which has low confidence in predicting the identity. Specifically, the identity is considered as a successful attack when the prediction score for the identity is lower than a threshold  $\gamma$ . In our experiment, the threshold  $\gamma$  is set to 0.6.

**Metrics.** Simultaneously, we use a series of metrics to explore the relation between the attack success rate and the intensity of proprietary morphing field. Specifically, we employ  $\ell_2$ -norm and  $\ell_{\infty}$ -norm as metrics to measure the intensity of proprietary morphing fields.

Adversarial morphing attack. In morphing facial images with learned proprietary morphing fields, we need to identify the range of the intensity of morphing fields and control them to investigate the relation between attack success rate. We first obtain the range of the intensity of morphing fields from the raw morphing fields which have successfully attack the FR systems in the query stage. The intensity of morphing fields are measured with  $\ell_2$ -norm and  $\ell_\infty$ -norm. To investigate the distribution of the intensity of raw morphing fields, we find that most of the  $\ell_2$ -norm and  $\ell_\infty$ -norm value lie in a fixed range.

$\mathcal{M}ackslash\ell_2$ 2	4	6	8	10	100	110	120	130	140	150	160	170	180	190	200	300	400	500	600
VGG-Face (VGG16) 0.341	0.341	0.341	0.341	0.341	0.500	0.477	0.500	0.523	0.568	0.523	0.523	0.545	0.523	0.523	0.523	0.591	0.614	0.614	0.614
VGG-Face (ResNet50) 0.024	0.024	0.014	0.010	0.014	0.082	0.106	0.101	0.115	0.120	0.115	0.125	0.130	0.135	0.159	0.159	0.231	0.365	0.500	0.596

**Table 4:** Attack success rate with different intensity of proprietary morphing field measured by  $\ell_2$ -norm on two popular face recognition systems.

$\mathcal{M}\setminus\ell_{\infty}$   0.1	0.2	0.3	0.4	0.5	1.0	1.1	1.2	1.3	1.4	1.5	1.6	1.7	1.8	1.9	2.0	3.0	4.0	5.0	6.0
VGG-Face (VGG16) 0.341	0.341	0.318	0.318	0.341	0.409	0.386	0.455	0.477	0.409	0.477	0.500	0.477	0.500	0.500	0.455	0.545	0.523	0.591	0.545
VGG-Face (ResNet50) 0.014	0.014	0.014	0.024	0.024	0.043	0.043	0.067	0.063	0.067	0.072	0.072	0.072	0.063	0.067	0.082	0.120	0.178	0.173	0.230

**Table 5:** Attack success rate with different intensity of proprietary morphing field measured by  $\ell_{\infty}$ -norm on two popular face recognition systems.

$\mathcal{M} \setminus \delta$										
VGG-Face (VGG16)	0.295	0.341	0.386	0.364	0.455	0.432	0.410	0.386	0.455	0.409
VGG-Face (ResNet50	0.029	0.019	0.034	0.034	0.043	0.053	0.067	0.091	0.096	0.106

**Table 6:** Enhancing the intensity of proprietary morphing fields on the multiplier  $\delta$ .

Thus, the intensity of proprietary morphing fields is split into several groups to evaluate their effectiveness in attacking the target FR systems.

Assigning proprietary morphing fields. Table 4 and Table 5 consolidate the attack success rates vs. different intensity of proprietary optical flow field with  $\ell_2$ -norm and  $\ell_\infty$ -norm, respectively. The intensity of proprietary morphing fields is mainly split into three groups according to the distribution of the raw morphing fields.

In measuring the intensity of proprietary morphing fields with  $\ell_2$ -norm, the three groups of intensity are as follows. 1) the first group is [2,10] with a step value 2; 2) the second group is [100,200] with a step value 10; 3) the third group is [200,600] with a step value 100. In measuring the intensity of proprietary morphing fields with  $\ell_{\infty}$ -norm, the three groups of intensity are as follows. 1) the first group is [0.1,0.5] with a step value 0.1; 2) the second group is [1.0,2.0] with a step value 0.1; 3) the third group is [2.0,6.0] with a step value 1.0.

Figure 6 plots the relation between the attack success rate and the modulated flow field on  $\ell_2$ -norm and  $\ell_\infty$ -norm. We can find that the successful attack is increasing with the intensity of proprietary morphing field. Since the intensity range spans two orders of magnitude, we present the plots in Figure 6 in semi-log on the x-axis. Experimental results shown that VGG-Face with VGG16 as backend architecture is more vulnerable than VGG-Face with ResNet50 as backend architecture. Our adversarial morphing attack can give an attack success rate of nearly 60% in attacking the two popular FR systems, VGG-Face (VGG16) and VGG-Face (ResNet50). Additionally, we also explore the relation between the attack success rate and the modulated flow filed on the multiplier  $\delta$  for enhancing the intensity of proprietary morphing fields. The range of the multiplier  $\delta$  is 0.2 to 2.0 with a step value 0.2.

Table 6 presents the results of attack success rate and the intensity of proprietary morphing with multiplier  $\delta$ . Figure 5 plots a trend of the increase of the multiplier  $\delta$  and attack success rate. We can also find that VGG-Face with VGG16 as backend architecture is more vulnerable than VGG-Face with ResNet50 as backend architecture. In order to get an intuitive visualization of facial images morphed with proprietary morphing fields, we present some high-resolution visualization of original faces and morphed facial images with different intensity of morphing fields on  $\ell_2$ -norm,  $\ell_\infty$ -norm, and multiplier  $\delta$  in Appendix A.

#### 4.3. Evaluation of Transferabilities

In this section, we mainly discuss the transferabilities of our adversarial morphing attack. Transferability is an important feature in adversarial attack, which means a successful attack in one model could be transferred to other models with high successful attack rate. In our experiment, we demonstrated the effectiveness of our adversarial morphing attack by investigating the attack transferabilities between VGG-Face with VGG16 as backend architecture and VGG-Face with ResNet50 as backend architecture.

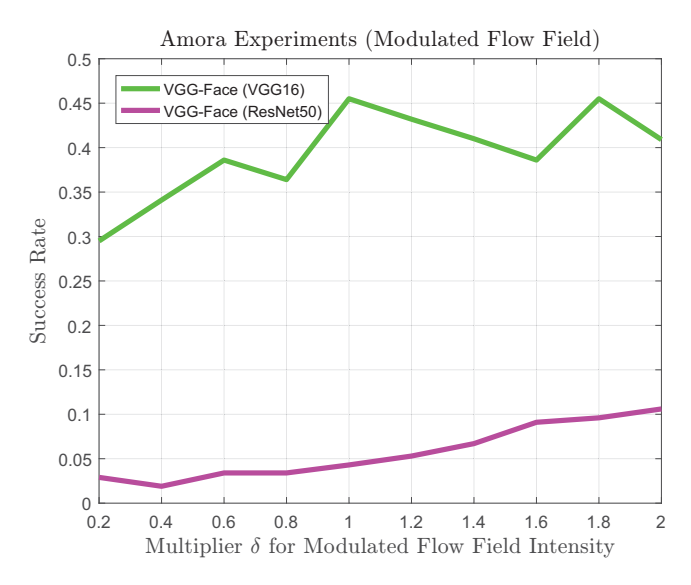


Figure 5: The relation between the attack success rate and the modulated flow field on the multiplier  $\delta$  for enhancing intensity.

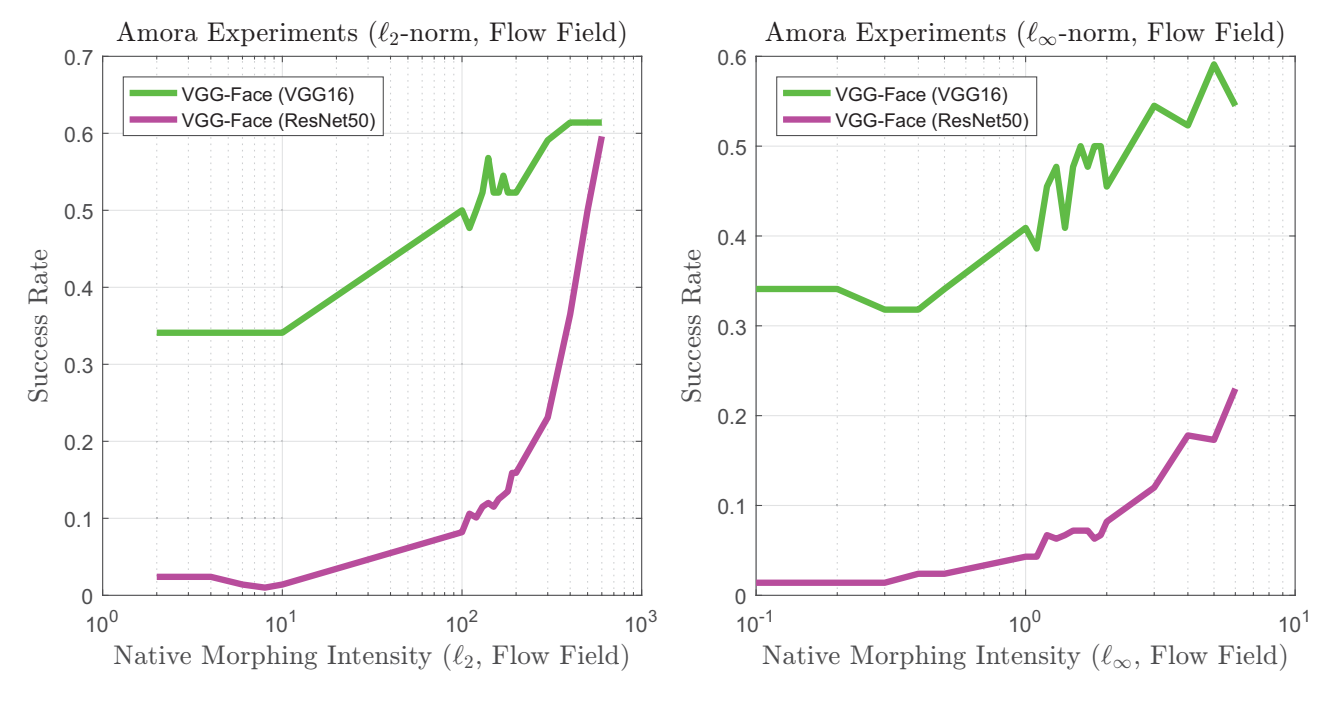


Figure 6: The relation between the attack success rate and the modulated flow field on  $\ell_2$ -norm &  $\ell_\infty$ -norm.

Our transferability evaluation experiments are conducted on a dataset from Table 2. Each facial image is morphed with their proprietary morphing field with  $\ell_2$ -norm and  $\ell_\infty$ -norm as metrics to control the intensity of morphing field. Table 7 presents us the experimental results in evaluating the transferabilities of adversarial morphing attack. The intensity of proprietary morphing field is measured by  $\ell_2$ -norm and  $\ell_\infty$ -norm and their value are presented in Table 4 and Table 5, respectively. Experimental results shown that our adversarial morphing attack gives an average 90% success rate in attacking transferabilities evaluation.

## 4.4. In Comparison with Baselines

In this section, we mainly discuss whether our proprietary morphing fields could be served as guidance in morphing facial images by comparing with several baselines which are generated in two ways, permuting proprietary morphing fields and generating morphing fields randomly with a specified value range. We compare the performance of our proprietary morphing

$metricsackslash\mathcal{M}$	VGG-Face (VGG16)	VGG-Face (ResNet50)
$\ell_2$ -norm	0.935	0.926
$\ell_{\infty}$ -norm	0.893	0.885

**Table 7:** The transferabilities of our proposed adversarial morphing attack between VGG-Face (VGG16) and VGG-Face (ResNet50) with  $\ell_2$ -norm and  $\ell_\infty$ -norm.

fields and baselines by exploring the relation between attack success rate and the intensity of morphing fields measured by  $\ell_2$ -norm and  $\ell_\infty$ -norm. Additionally, we also investigate the attack success rate and the visual quality of morphed facial images with SSIM and NCS.

**Permutation baseline.** In evaluating the performance of our learned proprietary morphing fields, we build a baseline by permuting the proprietary morphing fields while maintaining their intensity same as the original proprietary morphing fields. The proprietary morphing field includes two channels, horizontal channel  $\mathbf{f}^h$  and vertical channel  $\mathbf{f}^v$ . Thus, the permutation baseline could be permuted in two ways, permuting the morphing fields within channels, named intra-channel permutation baseline, and permuting the morphing fields between the two channels, named inter-channel permutation baseline.

Table 8, 10 and Table 12, 14 present the attack success rate with different intensity on proprietary morphing field and permutation baselines measured by  $\ell_2$ -norm and  $\ell_\infty$ -norm, respectively. We use green and blue colors to indicate the region of operation (ROO). ROO is the region where 'adversarial attack' assumption holds, *i.e.*, imperceptible to human eyes. Perturbation outside ROO causes very visible artifacts and is not meaningful in the context of adversarial attacks. Regions outside of ROO is marked in red color. A further distinction between green and blue is that the green color means that our proprietary morphing field performs better than the permutation baseline and the blue color denotes the performance of our proprietary morphing fields comparable to the permutation baseline.

Table 8 and Table 10 illustrate that our proprietary morphing field achieves higher or comparable attack success rate than the two permutation baselines when the morphing fields measured by  $\ell_2$ -norm is not larger than 300 and 170 in attacking the face recognition systems, VGG-Face with VGG16 and ResNet50 as backend, respectively. The permutation baseline outperforms our proprietary morphing fields when the value is larger than 400 and 200, respectively, but the morphed facial images appear significant visual artifacts with a heavy morphing as presented in Figure 7.

Table 12 and Table 14 demonstrate that our proprietary morphing field achieves higher or comparable attack success rate than the two permutation baselines when the morphing fields measured by  $\ell_{\infty}$ -norm is not larger than 5.0 and 4.0 in attacking the face recognition systems, VGG-Face with VGG16 and ResNet50 as backend, respectively. The permutation baseline outperforms our proprietary morphing fields when the value is larger than 5.0, but the morphed facial images appear significant visual artifacts as shown in Figure 7 and violate the basic assumption in adversarial attack, adversarial faces should be imperceptible to human eyes.

In summary, our proprietary morphing fields achieve higher attack success rate on  $\ell_2$ -norm and  $\ell_\infty$ -norm when the morphed facial images are imperceptible to human eyes with subtle morphing and without obvious visual artifacts. The permutation baseline outperforms our proprietary morphing field when the intensity of morphing fields measured by  $\ell_2$ -norm and  $\ell_\infty$ -norm are larger than a given value, but the morphed facial images appear significant visual artifacts and violate the basic assumption of adversarial attack.

Random baseline. We also build another baseline by randomly generating morphing field  $\mathbf{f}^h$  and  $\mathbf{f}^v$ , which follow a uniform distribution  $\mathcal{U}[-2,1]$ . The range value [-2,1] is determined by investigating the morphing fields which are successful in attacking the two FR systems in the query stage. There are more than 94.4% morphing fields lying in this range.  $\ell_2$ -norm and  $\ell_\infty$ -norm are employed to measure the intensity of morphing fields as well.

Table 9 and Table 11 illustrate that our proprietary morphing field achieves a higher or comparable attack success rate when the intensity of morphing fields measured by  $\ell_2$ -norm is not large than 300 in attacking two popular face recognition systems, VGG-Face with VGG16 and ResNet50 as backend. Table 13 and Table 15 demonstrate that our proprietary morphing field performs well than random baseline when the intensity of morphing fields measured by  $\ell_\infty$ -norm is lower than 3.0 and 1.8 in attacking the two popular face recognition systems.

The random baseline outperforms our proprietary morphing field in attacking the two popular face recognition systems when the intensity of the morphing field measured by  $\ell_2$ -norm is larger than 300 and the intensity measured by  $\ell_\infty$ -norm is larger than 2.0 and 1.7, respectively. However, the morphed facial images with heavy intensity of morphing fields would appear obvious visual artifacts as shown in Figure 7 and violate the basic assumption of adversarial attack. Thus, our proprietary

$\mathcal{M}ackslash\ell_2$	2	4	6	8	10	100	110	120	130	140	150	160	170	180	190	200	300	400	500	600
VGG-Face (VGG16)	0.341	0.341	0.341	0.341	0.341	0.500	0.477	0.500	0.523	0.568	0.523	0.523	0.545	0.523	0.523	0.523	0.591	0.614	0.614	0.614
Baseline (intra-channel)	0.341	0.341	0.341	0.341	0.341	0.364	0.364	0.409	0.432	0.364	0.341	0.386	0.386	0.409	0.409	0.455	0.523	0.545	0.659	0.682
Baseline (inter-channel)	0.364	0.341	0.341	0.341	0.341	0.341	0.364	0.386	0.409	0.432	0.386	0.386	0.364	0.432	0.455	0.455	0.568	0.727	0.795	0.864

**Table 8:** Attack success rate with different intensity on proprietary morphing filed and two baselines (*e.g.*, randomly permuting the proprietary morphing fields on *intra-channel* and *inter-channel*) on a popular face recognition system, VGG-Face with VGG16 as backend. The intensity of proprietary morphing field and two baselines is measured by  $\ell_2$ -norm.

morphing filed also performs better than the random baseline in attacking the two popular face recognition systems when the morphed facial images appear subtle visual artifacts and imperceptible to human eyes.

Negative results on random baseline. In Table 15, the attack success rate in most of the regions is comparable to the baseline  $\mathcal{U}[-2,1]$  and  $\mathcal{U}[-1,1]$  as the variance within our proprietary morphing fields is larger than the two baselines and it dominates the  $\ell_{\infty}$ -norm value. Thus, the intensity of our proprietary morphing fields is minor than the two baselines under the same  $\ell_{\infty}$ -norm value. In our experiment, we build another baseline, randomly generating morphing fields with gaussian distribution  $\mathcal{N}[0,1]$ , for evaluating the performance of our proprietary morphing filed measured by  $\ell_{\infty}$ -norm in attacking VGG-Face with ResNet50 as backend. Experimental results show that our proprietary morphing fields achieve a higher or comparable attack success rate than the baseline when the  $\ell_{\infty}$ -norm value is lower than 5.0.

In comparison with the two baselines, permutation baseline and random baseline, our learned proprietary morphing filed shows its power in evading face recognition systems by morphing facial images while the morphed facial images are still imperceptible to human eyes. However, the two chosen baselines are considered strong baselines as they capitalize on the prior knowledge of what optical flow fields should be. For example, the permutation baseline leverages the proprietary flow field as a starting point for the random permutation process in the case of inter-channel and intra-channel permutation baselines, or the random baseline utilizes the value range of all computed proprietary flow fields. It is interesting to explore some moderate baselines in our future work.

Similarity measurement. To present a comprehensive evaluation of our proprietary morphing field in comparison with baselines, we explore the attack success rate and visual quality of morphed facial images measured by two typical similarity distance metrics, SSIM and NCS. Specifically, we build a random baseline by randomly generating morphing fields that follows three different distributions, uniform distribution  $\mathcal{U}[-2,1]$  and  $\mathcal{U}[-1,1]$  and gaussian distribution  $\mathcal{N}(0,1)$ . Table 16 and Table 17 present the experimental result in comparing with baselines where the similarity distance between original facial image and morphed facial images is measured with SSIM and NCS.

In Table 16, we divide the region into eight groups according to the distribution of the SSIM between original facial image and morphed facial image with proprietary morphing field and random baseline. The larger SSIM means the original facial image and morphed facial image are similar. Table 16 indicates that our proprietary morphing fields achieve a high attack success rate when the morphed facial images are similar to original facial images, especially the SSIM value is larger than 0.9.

We employ another different similarity distance metric, NCS, for evaluating the performance of our proprietary morphing field in attacking face recognition systems. Table 17 illustrates a similar results as Table 16 using SSIM. Our proprietary morphing field also achieves high attack success rate when NCS is larger than 0.998. Thus, our proprietary morphing field performs better than the random baseline in attacking face recognition systems when the morphed facial images with subtle changes and imperceptible to human eyes.

In comparison with several our build baselines and evaluating with two perceptual metrics, experimental results demonstrated that our learned proprietary can be well served as an effective guidance in morphing facial images to attack face recognition systems by considering both the attack success rate and the quality of morphed facial images which appears less visual artifacts.

#### 4.5. Open-set Evaluation

As open-set face recognition is common, we have evaluated the effectiveness of our approach in attacking close-set FR systems. In this section, we present the experimental results of our adversarial morphing attacking in dealing with open-set attack where focus on unseen classes.

We trained two popular FR systems with 500 identities on *CelebA-HQ* dataset, namely VGG-Face with VGG16 as backend and VGG-Face with ResNet50 as backend. In testing, the identity of a new given face is unseen in training. In experiment, we



Figure 7: Samples of morphed facial images with different baselines. The first three rows represent the morphing fields measured by  $\ell_2$ -norm (values are 180, 190, 200, 300, 400, 500, 600 from the left to right) and the morphed facial images are morphed with permutation baseline on *inter-channel*, permutation baseline on *inter-channel*, and random baseline. The last three rows represent the morphing fields measured by  $\ell_\infty$ -norm (values are 1.7, 1.8, 1.9, 2.0, 3.0, 4.0, 5.0 from the left to right) and the morphed facial images are morphed with permutation baseline on *intra-channel*, permutation baseline on *inter-channel*, and random baseline. Morphed facial images with red frame denote the image has obvious artifacts.

$\mathcal{M}ackslash\ell_2$   2	4	6	8	10	100	110	120	130	140	150	160	170	180	190	200	300	400	500	600
VGG-Face (VGG16) 0.341	0.341	0.341	0.341	0.341	0.500	0.477	0.500	0.523	0.568	0.523	0.523	0.545	0.523	0.523	0.523	0.591	0.614	0.614	0.614
Baseline $\mathcal{U}[-2,1]$ 0.318	0.318	0.295	0.295	0.295	0.364	0.409	0.432	0.386	0.455	0.432	0.455	0.477	0.477	0.477	0.5	0.568	0.705	0.818	0.909

**Table 9:** Attack success rate with different intensity on proprietary morphing field and a baseline (randomly generating morphing fields follows an uniform distribution  $\mathcal{U}[-2,1]$ ) on a popular face recognition system, VGG-Face with VGG16 as backend. The intensity of proprietary morphing field and the baseline is measured by  $\ell_2$ -norm.

evaluate whether our morphed facial images with assigned proprietary morphing fields decrease the performance of open-set FR systems in classification.

We use ROC curve to evaluate the performance of our adversarial morphing attack in attacking open-set FR systems. ROC curve is an important and common method for evaluating the performance of classifiers. Verification rate (VR) at 0.001 false accept rate (FAR), equal error rate (EER), and area under the ROC curve (AUC) are adopted as verification scores for

$\mathcal{M}ackslash\ell_2$	2	4	6	8	10	100	110	120	130	140	150	160	170	180	190	200	300	400	500	600
VGG-Face (ResNet50)	0.024	0.024	0.014	0.010	0.014	0.082	0.106	0.101	0.115	0.120	0.115	0.125	0.130	0.135	0.159	0.159	0.231	0.365	0.500	0.596
Baseline (intra-channel)	0.019	0.014	0.019	0.019	0.024	0.067	0.082	0.082	0.082	0.091	0.091	0.111	0.115	0.154	0.149	0.168	0.356	0.524	0.663	0.798
Baseline (inter-channel)	0.014	0.024	0.014	0.014	0.014	0.082	0.096	0.096	0.101	0.101	0.091	0.106	0.115	0.139	0.139	0.159	0.313	0.495	0.668	0.803

**Table 10:** Attack success rate with different intensity on proprietary morphing filed and two baselines (*e.g.*, randomly permuting the proprietary morphing fields on *intra-channel* and *inter-channel*) on a popular face recognition system, VGG-Face with ResNet50 as backend. The intensity of proprietary morphing field and two baselines is measured by  $\ell_2$ -norm.

$\mathcal{M}ackslash\ell_2$ 2	4	6	8	10	100	110	120	130	140	150	160	170	180	190	200	300	400	500	600
VGG-Face (ResNet50) 0.024	0.024	0.014	0.010	0.014	0.082	0.106	0.101	0.115	0.120	0.115	0.125	0.130	0.135	0.159	0.159	0.231	0.365	0.500	0.596
Baseline $\mathcal{U}[-2,1]$ 0.024	0.024	0.034	0.024	0.034	0.106	0.101	0.106	0.106	0.096	0.101	0.120	0.144	0.149	0.154	0.144	0.298	0.524	0.697	0.832

Table 11: Attack success rate with different intensity on proprietary morphing field and a baseline (randomly generating morphing fields follows an uniform distribution  $\mathcal{U}[-2,1]$ ) on a popular face recognition system, VGG-Face with ResNet50 as backend. The intensity of proprietary morphing field and the baseline is measured by  $\ell_2$ -norm.

$\mathcal{M}ackslash\ell_{\infty}$	0.1	0.2	0.3	0.4	0.5	1.0	1.1	1.2	1.3	1.4	1.5	1.6	1.7	1.8	1.9	2.0	3.0	4.0	5.0	6.0
VGG-Face (VGG16) 0	.341	0.341	0.318	0.318	0.341	0.409	0.386	0.455	0.477	0.409	0.477	0.500	0.477	0.500	0.500	0.455	0.545	0.523	0.591	0.545
Baseline (intra-channel) 0	.341	0.318	0.295	0.318	0.341	0.295	0.341	0.341	0.364	0.364	0.295	0.386	0.341	0.364	0.364	0.386	0.409	0.455	0.5	0.568
Baseline (inter-channel) 0	.318	0.318	0.295	0.341	0.273	0.273	0.295	0.318	0.295	0.341	0.364	0.295	0.364	0.318	0.318	0.364	0.341	0.477	0.614	0.614

**Table 12:** Attack success rate with different intensity on proprietary morphing filed and two baselines (*e.g.*, randomly permuting the proprietary morphing fields on *intra-channel* and *inter-channel*) on a popular face recognition system, VGG-Face with VGG16 as backend. The intensity of proprietary morphing field and two baselines is measured by  $\ell_{\infty}$ -norm.

$\mathcal{M}\setminus\ell_{\infty}$   0.1	0.2	0.3	0.4	0.5	1.0	1.1	1.2	1.3	1.4	1.5	1.6	1.7	1.8	1.9	2.0	3.0	4.0	5.0	6.0
VGG-Face (VGG16) 0.341	0.341	0.318	0.318	0.341	0.409	0.386	0.455	0.477	0.409	0.477	0.500	0.477	0.500	0.500	0.455	0.545	0.523	0.591	0.545
Baseline $\mathcal{U}[-2,1]$ 0.364	0.341	0.318	0.318	0.341	0.409	0.409	0.455	0.432	0.432	0.409	0.432	0.432	0.432	0.455	0.455	0.613	0.727	0.773	0.795

Table 13: Attack success rate with different intensity on proprietary morphing field and a baseline (randomly generating morphing fields follows an uniform distribution  $\mathcal{U}[-2,1]$ ) on a popular face recognition system, VGG-Face with VGG16 as backend. The intensity of proprietary morphing field and the baseline is measured by  $\ell_{\infty}$ -norm.

$\mathcal{M}ackslash\ell_\infty$	0.1	0.2	0.3	0.4	0.5	1.0	1.1	1.2	1.3	1.4	1.5	1.6	1.7	1.8	1.9	2.0	3.0	4.0	5.0	6.0
VGG-Face (ResNet50)	0.014	0.014	0.014	0.024	0.024	0.043	0.043	0.067	0.063	0.067	0.072	0.072	0.072	0.063	0.067	0.082	0.120	0.178	0.173	0.230
Baseline (intra-channel)	0.024	0.019	0.024	0.024	0.014	0.058	0.063	0.072	0.067	0.063	0.053	0.063	0.077	0.077	0.087	0.091	0.139	0.197	0.279	0.341
Baseline (inter-channel)	0.019	0.024	0.019	0.038	0.024	0.043	0.053	0.058	0.058	0.053	0.058	0.062	0.067	0.077	0.072	0.082	0.106	0.178	0.288	0.361

**Table 14:** Attack success rate with different intensity on proprietary morphing filed and two baselines (*e.g.*, randomly permuting the proprietary morphing fields on *intra-channel* and *inter-channel*) on a popular face recognition system, VGG-Face with ResNet50 as backend. The intensity of proprietary morphing field and two baselines is measured by  $\ell_{\infty}$ -norm.

evaluating the performance of our adversarial morphing attack in attacking open-set FR systems. Higher EER means higher attack success rate while lower VR and AUC mean higher attack success rate.

$\mathcal{M}ackslash\ell_{\infty}$   0.1	0.2	0.3	0.4	0.5	1.0	1.1	1.2	1.3	1.4	1.5	1.6	1.7	1.8	1.9	2.0	3.0	4.0	5.0	6.0
VGG-Face (ResNet50) 0.014	0.014	0.014	0.024	0.024	0.043	0.043	0.067	0.063	0.067	0.072	0.072	0.072	0.063	0.067	0.082	0.120	0.178	0.173	0.230
Baseline $\mathcal{U}[-2,1]$ 0.024	0.019	0.029	0.034	0.048	0.058	0.058	0.063	0.082	0.072	0.082	0.082	0.091	0.115	0.101	0.101	0.250	0.409	0.567	0.731
Baseline $\mathcal{U}[-1,1]$ 0.038	0.019	0.014	0.010	0.034	0.096	0.106	0.130	0.135	0.149	0.168	0.163	0.173	0.188	0.178	0.197	0.457	0.745	0.865	0.957
Baseline $\mathcal{N}[0,1]$ 0.034	0.034	0.043	0.038	0.043	0.024	0.029	0.043	0.034	0.048	0.038	0.048	0.048	0.058	0.063	0.048	0.082	0.130	0.197	0.245

**Table 15:** Attack success rate with different intensity on proprietary morphing field and three baseline (randomly generating morphing fields follows uniform distribution  $\mathcal{U}[-2,1]$ ,  $\mathcal{U}[-1,1]$ , and gaussian distribution  $\mathcal{N}[0,1]$ ) on a popular face recognition system, VGG-Face with ResNet50 as backend. The intensity of proprietary morphing field and the baseline is measured by  $\ell_{\infty}$ -norm.

$\mathcal{M} \backslash ssim$	[0.5, 0.6)	[0.6, 0.7)	[0.7, 0.75)	[0.75, 0.8)	[0.8, 0.85)	[0.85, 0.9)	[0.9, 0.95)	[0.95, 1.0]
VGG-Face (VGG16)	0	0	0	0	0	0.048	0.073	0.373
Baseline $\mathcal{U}[-2,1]$ (VGG16)	0	0	0.333	0.278	0.128	0.079	0.032	0.046
Baseline $\mathcal{U}[-1,1]$ (VGG16)	0	0	0.036	0.346	0.181	0.104	0.073	0.035
Baseline $\mathcal{N}(0,1)$ (VGG16)	0	0.003	0.424	0.224	0.123	0.07	0.016	0.032
VGG-Face (ResNet50)	0	0	0	0	0.0002	0.052	0.034	0.070
Baseline $\mathcal{U}[-2,1]$ (ResNet50)	0	0	0.347	0.246	0.141	0.05	0.004	0.020
Baseline $\mathcal{U}[-1, 1]$ (ResNet50)	0	0	0.055	0.321	0.181	0.106	0.046	0.007
Baseline $\mathcal{N}(0,1)$ (ResNet50)	0	0.002	0.445	0.220	0.106	0.059	0.005	0.012

**Table 16:** Attack success rate and perceptual similarity measurement with SSIM in comparing with three random baselines,  $\mathcal{U}[-2,1]$ ,  $\mathcal{U}[-1,1]$ , and  $\mathcal{N}(0,1)$ .

$\mathcal{M} \backslash ncs$	[0.982, 0.984)	[0.984, 0.986)	[0.986, 0.988)	[0.988, 0.990]	[0.990, 0.992)	[0.992, 0.994)	[0.994, 0.996)	[0.996, 0.998)	[0.998, 1.0]
VGG-Face (VGG16)	0	0	0	0	0	0.001	0.014	0.058	0.420
Baseline $\mathcal{U}[-2,1]$ (VGG16)	0	0	0.003	0.008	0.032	0.091	0.185	0.355	0.222
Baseline $\mathcal{U}[-1,1]$ (VGG16)	0	0	0	0	0	0.006	0.046	0.279	0.444
Baseline $\mathcal{N}(0,1)$ (VGG16)	0	0	0	0.003	0.008	0.052	0.151	0.366	0.312
VGG-Face (ResNet50)	0	0	0	0.0005	0.0012	0.005	0.018	0.041	0.090
Baseline $\mathcal{U}[-2,1]$ (ResNet50)	0	0.005	0.018	0.040	0.065	0.134	0.189	0.241	0.116
Baseline $\mathcal{U}[-1,1]$ (ResNet50)	0	0	0	0	0.001	0.023	0.113	0.278	0.300
Baseline $\mathcal{N}(0,1)$ (ResNet50)	0	0	0.001	0.012	0.034	0.097	0.191	0.303	0.210

**Table 17:** Attack success rate and perceptual similarity measurement with NCS in comparing with three random baselines,  $\mathcal{U}[-2,1]$ ,  $\mathcal{U}[-1,1]$ , and  $\mathcal{N}(0,1)$ .

Table 18 and Table 19 present us the open-set face verification scores with 20 different intensity on proprietary morphing field measured by  $\ell_2$ -norm on ResNet-50 and VGG-16 face recognition systems, respectively. The two popular face recognition systems are more easily to be attacked when the intensity of proprietary morphing fields increased according to the face verification scores VR, EER, and AUC.

Scores $\setminus \ell_2$	2	4	6	8	10	100	110	120	130	140	150	160	170	180	190	200	300	400	500	600   Orig.
VR	93.37	93.33	93.31	93.28	93.26	92.88	92.82	92.53	92.61	92.44	92.28	92.13	91.50	91.44	91.32	90.43	85.19	79.01	71.73	64.49   93.38
EER	1.52	1.52	1.52	1.52	1.52	1.31	1.30	1.36	1.35	1.42	1.42	1.49	1.47	1.45	1.49	1.52	1.79	2.33	3.13	4.21   1.52
AUC	99.64	99.64	99.64	99.64	99.64	99.63	99.63	99.64	99.63	99.63	99.62	99.62	99.62	99.62	99.61	99.61	99.58	99.50	99.36	99.18   99.64

**Table 18:** Open-set face verification scores (verification rate (VR) at 0.001 false accept rate (FAR), equal error rate (EER), and area under the ROC curves (AUC)) with different intensity on proprietary morphing field measured by  $\ell_2$ -norm on ResNet-50 face recognition systems.

Scores $\setminus \ell_2$	2	4	6	8	10	100	110	120	130	140	150	160	170	180	190	200	300	400	500	600   Orig.
VR	94.33	94.34	94.40	94.38	94.36	94.71	94.74	94.76	94.80	94.78	94.83	94.80	94.73	94.73	94.64	94.66	93.71	91.83	87.52	82.66   94.69
EER	1.48	1.46	1.47	1.44	1.44	1.48	1.49	1.55	1.54	1.54	1.58	1.59	1.60	1.59	1.63	1.66	1.70	1.80	2.13	2.73   1.42
AUC	99.64	99.64	99.64	99.64	99.65	99.68	99.68	99.69	99.69	99.69	99.69	99.69	99.69	99.69	99.69	99.69	99.71	99.70	99.66	99.56   99.62

**Table 19:** Open-set face verification scores (verification rate (VR) at 0.001 false accept rate (FAR), equal error rate (EER), and area under the ROC curves (AUC)) with different intensity on proprietary morphing field measured by  $\ell_2$ -norm on VGG-16 face recognition systems.

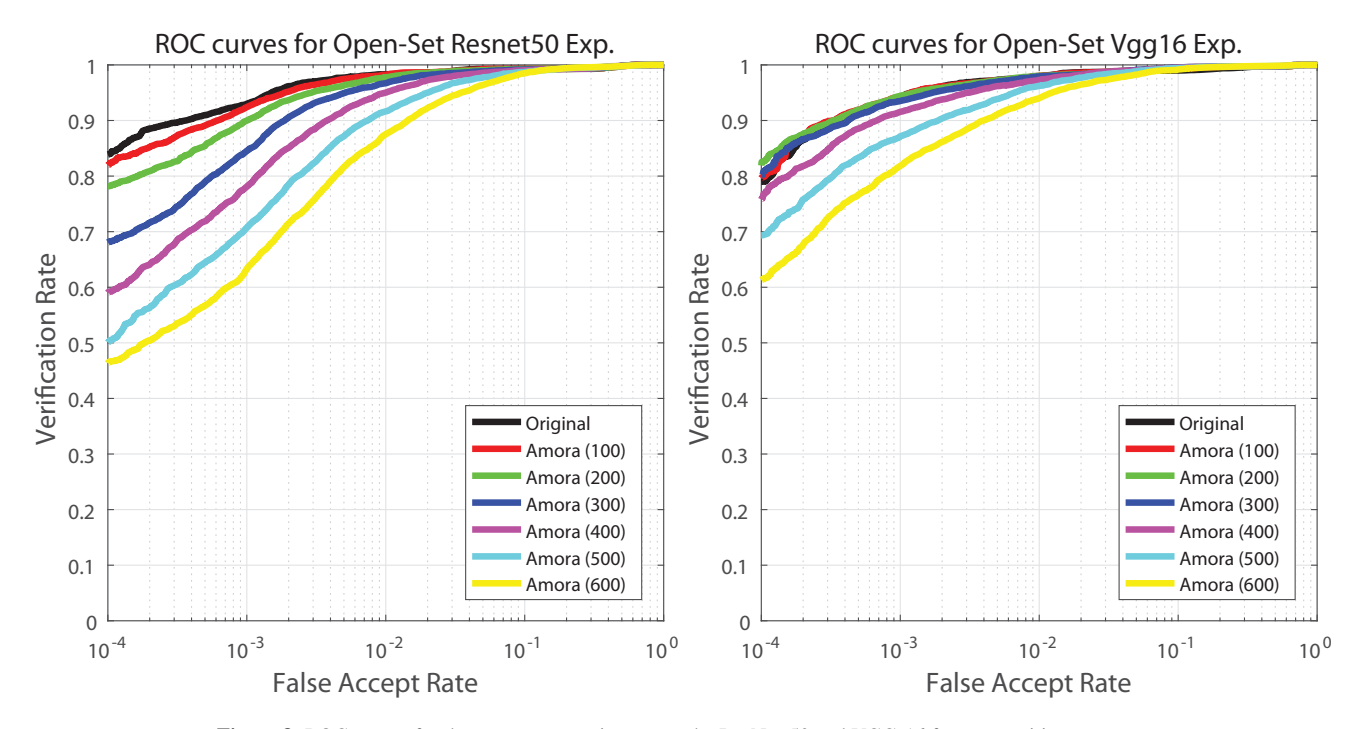


Figure 8: ROC curves for the open-set experiments on the ResNet-50 and VGG-16 face recognition systems.

Figure 8 (L) and (R) show us the ROC curves for the open-set experiments on the ResNet-50 and VGG-16 face recognition systems, respectively. In Figure 8, we select six different intensity on proprietary morphing field measured by  $\ell_2$ -norm to generate morphed facial images for attacking ResNet-50 and VGG-16 face recognition systems. The lower AUC means the face recognition system is more easily to be attacked. In comparing with the original facial images, we find that our morphed facial images on different intensity proprietary morphing fields can achieve more success attack possibilities in attacking open-set face recognition systems.

### 5. Conclusions

In this work, we have introduced and investigated a new type of black-box adversarial attack to evade deep-learning based FR systems by morphing facial images with optical flows. The proposed attack morphs/deforms pixels spatially as opposed to adversarial noise attack that perturbs the pixel intensities.

With a simple yet effective learning pipeline, we are able to obtain a proprietary morphing field for each individual attack. Experimental results have shown that some popular FR systems can be evaded with high probability and the performance of

these systems is significantly decreased with our attacks. Our observation has raised an essential security issue in currently deployed FR systems. Through comprehensive experiments and validations, we have shown that a black-box adversarial morphing attack is not only possible, but also compromises the FR systems significantly.

The proposed black-box adversarial morphing attack points to an orthogonal direction that can complement the existing adversarial noise attacks. Therefore, it is possible to combine various attack types in the future. Also, while presentation spoofing attacks are relatively easier to defend because they rely heavily on physical props, and adversarial noise attacks are less likely to be presented in real-world setups, it is useful to study the physical attacks based on adversarial morphing, since it is a semantically coherent attack with local facial deformation and is likely to happen in real scenarios.

## 6. Acknowledgement

We gratefully acknowledge the support of NVIDIA AI Tech Center (NVAITC) to our research.

### References

- [1] Rima Alaifari, Giovanni S Alberti, and Tandri Gauksson. Adef: an iterative algorithm to construct adversarial deformations. *arXiv* preprint arXiv:1804.07729, 2018. 4
- [2] Battista Biggio, Igino Corona, Davide Maiorca, Blaine Nelson, Nedim Šrndić, Pavel Laskov, Giorgio Giacinto, and Fabio Roli. Evasion attacks against machine learning at test time. In *Joint European conference on machine learning and knowledge discovery in databases*, pages 387–402. Springer, 2013. 1, 3
- [3] BioID. BioID Face Liveness Detection. https://www.bioid.com/liveness-detection/. Accessed: 2019-11-11. 2
- [4] Avishek Joey Bose and Parham Aarabi. Adversarial attacks on face detectors using neural net based constrained optimization. In 2018 IEEE 20th International Workshop on Multimedia Signal Processing (MMSP), pages 1–6. IEEE, 2018. 4
- [5] Nicholas Carlini and David Wagner. Towards evaluating the robustness of neural networks. In 2017 IEEE Symposium on Security and Privacy (SP), pages 39–57. IEEE, 2017. 3
- [6] Pin-Yu Chen, Huan Zhang, Yash Sharma, Jinfeng Yi, and Cho-Jui Hsieh. Zoo: Zeroth order optimization based black-box attacks to deep neural networks without training substitute models. In *Proceedings of the 10th ACM Workshop on Artificial Intelligence and Security*, pages 15–26. ACM, 2017. 3
- [7] Debayan Deb, Jianbang Zhang, and Anil K Jain. Advfaces: Adversarial face synthesis. arXiv preprint arXiv:1908.05008, 2019. 2, 4
- [8] Yinpeng Dong, Hang Su, Baoyuan Wu, Zhifeng Li, Wei Liu, Tong Zhang, and Jun Zhu. Efficient decision-based black-box adversarial attacks on face recognition. In *Proceedings of the IEEE Conference on Computer Vision and Pattern Recognition*, pages 7714–7722, 2019. 4
- [9] Xiaoning Du, Xiaofei Xie, Yi Li, Lei Ma, Yang Liu, and Jianjun Zhao. Deepstellar: model-based quantitative analysis of stateful deep learning systems. In *Proceedings of the 2019 27th ACM Joint Meeting on European Software Engineering Conference and Symposium on the Foundations of Software Engineering*, pages 477–487. ACM, 2019. 3
- [10] Javid Ebrahimi, Anyi Rao, Daniel Lowd, and Dejing Dou. Hotflip: White-box adversarial examples for text classification. *arXiv* preprint arXiv:1712.06751, 2017. 1
- [11] Ian Goodfellow, Jean Pouget-Abadie, Mehdi Mirza, Bing Xu, David Warde-Farley, Sherjil Ozair, Aaron Courville, and Yoshua Bengio. Generative adversarial nets. In *Advances in neural information processing systems*, pages 2672–2680, 2014. 3
- [12] Ian J Goodfellow, Jonathon Shlens, and Christian Szegedy. Explaining and harnessing adversarial examples. *arXiv preprint* arXiv:1412.6572, 2014. 1, 2, 3
- [13] Kathrin Grosse, Nicolas Papernot, Praveen Manoharan, Michael Backes, and Patrick McDaniel. Adversarial examples for malware detection. In *European Symposium on Research in Computer Security*, pages 62–79. Springer, 2017. 1
- [14] E. Ilg, N. Mayer, T. Saikia, M. Keuper, A. Dosovitskiy, and T. Brox. Flownet 2.0: Evolution of optical flow estimation with deep networks. In *IEEE Conference on Computer Vision and Pattern Recognition (CVPR)*, Jul 2017. 7
- [15] Andrew Ilyas, Logan Engstrom, Anish Athalye, and Jessy Lin. Black-box adversarial attacks with limited queries and information. arXiv preprint arXiv:1804.08598, 2018. 3
- [16] Felix Juefei-Xu, Dipan K Pal, and Marios Savvides. Hallucinating the full face from the periocular region via dimensionally weighted k-svd. In *Proceedings of the IEEE Conference on Computer Vision and Pattern Recognition Workshops*, pages 1–8, 2014. 6
- [17] Felix Juefei-Xu, Dipan K Pal, and Marios Savvides. Nir-vis heterogeneous face recognition via cross-spectral joint dictionary learning and reconstruction. In *Proceedings of the IEEE conference on computer vision and pattern recognition workshops*, pages 141–150, 2015. 6
- [18] Felix Juefei-Xu and Marios Savvides. Encoding and decoding local binary patterns for harsh face illumination normalization. In 2015 IEEE International Conference on Image Processing (ICIP), pages 3220–3224. IEEE, 2015. 6
- [19] Felix Juefei-Xu and Marios Savvides. Pokerface: partial order keeping and energy repressing method for extreme face illumination normalization. In 2015 IEEE 7th International Conference on Biometrics Theory, Applications and Systems (BTAS), pages 1–8. IEEE, 2015. 6
- [20] Felix Juefei-Xu and Marios Savvides. Fastfood dictionary learning for periocular-based full face hallucination. In 2016 IEEE 8th International Conference on Biometrics Theory, Applications and Systems (BTAS), pages 1–8. IEEE, 2016. 6
- [21] Felix Juefei-Xu and Marios Savvides. Learning to invert local binary patterns. In BMVC, 2016. 6
- [22] Tero Karras, Timo Aila, Samuli Laine, and Jaakko Lehtinen. Progressive growing of gans for improved quality, stability, and variation. arXiv preprint arXiv:1710.10196, 2017.
- [23] Tero Karras, Samuli Laine, and Timo Aila. A style-based generator architecture for generative adversarial networks. In *Proceedings of the IEEE Conference on Computer Vision and Pattern Recognition*, pages 4401–4410, 2019.
- [24] Jinhan Kim, Robert Feldt, and Shin Yoo. Guiding deep learning system testing using surprise adequacy. In *Proceedings of the 41st International Conference on Software Engineering*, ICSE '19, pages 1039–1049, 2019. 3
- [25] Neslihan Kose and Jean-Luc Dugelay. On the vulnerability of face recognition systems to spoofing mask attacks. In 2013 IEEE International Conference on Acoustics, Speech and Signal Processing, pages 2357–2361. IEEE, 2013. 2
- [26] Alexander Levine and Soheil Feizi. Wasserstein smoothing: Certified robustness against wasserstein adversarial attacks. *arXiv preprint* arXiv:1910.10783, 2019. 4

- [27] Ziwei Liu, Ping Luo, Xiaogang Wang, and Xiaoou Tang. Deep learning face attributes in the wild. In *Proceedings of International Conference on Computer Vision (ICCV)*, December 2015. 7
- [28] Lei Ma, Felix Juefei-Xu, Minhui Xue, Bo Li, Li Li, Yang Liu, and Jianjun Zhao. Deepct: Tomographic combinatorial testing for deep learning systems. In 2019 IEEE 26th International Conference on Software Analysis, Evolution and Reengineering (SANER), pages 614–618. IEEE, 2019. 3
- [29] Lei Ma, Felix Juefei-Xu, Fuyuan Zhang, Jiyuan Sun, Minhui Xue, Bo Li, Chunyang Chen, Ting Su, Li Li, Yang Liu, et al. Deepgauge: Multi-granularity testing criteria for deep learning systems. In *Proceedings of the 33rd ACM/IEEE International Conference on Automated Software Engineering*, pages 120–131. ACM, 2018. 3
- [30] Lei Ma, Fuyuan Zhang, Jiyuan Sun, Minhui Xue, Bo Li, Felix Juefei-Xu, Chao Xie, Li Li, Yang Liu, Jianjun Zhao, et al. Deepmutation: Mutation testing of deep learning systems. In 2018 IEEE 29th International Symposium on Software Reliability Engineering (ISSRE), pages 100–111. IEEE, 2018. 4
- [31] Aleksander Madry, Aleksandar Makelov, Ludwig Schmidt, Dimitris Tsipras, and Adrian Vladu. Towards deep learning models resistant to adversarial attacks. *arXiv preprint arXiv:1706.06083*, 2017. 2
- [32] Seyed-Mohsen Moosavi-Dezfooli, Alhussein Fawzi, and Pascal Frossard. Deepfool: a simple and accurate method to fool deep neural networks. In *Proceedings of the IEEE conference on computer vision and pattern recognition*, pages 2574–2582, 2016. 3
- [33] Nina Narodytska and Shiva Kasiviswanathan. Simple black-box adversarial attacks on deep neural networks. In 2017 IEEE Conference on Computer Vision and Pattern Recognition Workshops (CVPRW), pages 1310–1318. IEEE, 2017. 3
- [34] Augustus Odena, Catherine Olsson, David Andersen, and Ian Goodfellow. TensorFuzz: Debugging neural networks with coverage-guided fuzzing. In Kamalika Chaudhuri and Ruslan Salakhutdinov, editors, *Proceedings of the 36th International Conference on Machine Learning*, volume 97 of *Proceedings of Machine Learning Research*, pages 4901–4911, Long Beach, California, USA, 09–15 Jun 2019. PMLR. 3
- [35] Nicolas Papernot, Patrick McDaniel, Ian Goodfellow, Somesh Jha, Z Berkay Celik, and Ananthram Swami. Practical black-box attacks against machine learning. In *Proceedings of the 2017 ACM on Asia conference on computer and communications security*, pages 506–519. ACM, 2017. 3
- [36] Nicolas Papernot, Patrick McDaniel, Somesh Jha, Matt Fredrikson, Z Berkay Celik, and Ananthram Swami. The limitations of deep learning in adversarial settings. In 2016 IEEE European Symposium on Security and Privacy (EuroS&P), pages 372–387. IEEE, 2016.
- [37] Kexin Pei, Yinzhi Cao, Junfeng Yang, and Suman Jana. Deepxplore: Automated whitebox testing of deep learning systems. In *Proceedings of the 26th Symposium on Operating Systems Principles*, pages 1–18. ACM, 2017. 3
- [38] Anurag Ranjan, Joel Janai, Andreas Geiger, and Michael J Black. Attacking optical flow. In *Proceedings of the IEEE International Conference on Computer Vision*, pages 2404–2413, 2019. 4
- [39] Fitsum Reda, Robert Pottorff, Jon Barker, and Bryan Catanzaro. flownet2-pytorch: Pytorch implementation of flownet 2.0: Evolution of optical flow estimation with deep networks. https://github.com/NVIDIA/flownet2-pytorch, 2017. 7
- [40] Mahmood Sharif, Sruti Bhagavatula, Lujo Bauer, and Michael K Reiter. Accessorize to a crime: Real and stealthy attacks on state-of-the-art face recognition. In *Proceedings of the 2016 ACM SIGSAC Conference on Computer and Communications Security*, pages 1528–1540. ACM, 2016. 1, 2, 4
- [41] Qing Song, Yingqi Wu, and Lu Yang. Attacks on state-of-the-art face recognition using attentional adversarial attack generative network. arXiv preprint arXiv:1811.12026, 2018. 4
- [42] Run Wang, Lei Ma, Felix Juefei-Xu, Xiaofei Xie, Jian Wang, and Yang Liu. Fakespotter: A simple baseline for spotting ai-synthesized fake faces. *arXiv preprint arXiv:1909.06122*, 2019. 4
- [43] Svante Wold, Kim Esbensen, and Paul Geladi. Principal component analysis. *Chemometrics and intelligent laboratory systems*, 2(1-3):37–52, 1987. 5
- [44] Eric Wong, Frank R Schmidt, and J Zico Kolter. Wasserstein adversarial examples via projected sinkhorn iterations. *arXiv preprint arXiv:1902.07906*, 2019. 4
- [45] Chaowei Xiao, Jun-Yan Zhu, Bo Li, Warren He, Mingyan Liu, and Dawn Song. Spatially transformed adversarial examples. *arXiv* preprint arXiv:1801.02612, 2018. 4
- [46] Xiaofei Xie, Lei Ma, Felix Juefei-Xu, Minhui Xue, Hongxu Chen, Yang Liu, Jianjun Zhao, Bo Li, Jianxiong Yin, and Simon See. Deephunter: a coverage-guided fuzz testing framework for deep neural networks. In *Proceedings of the 28th ACM SIGSOFT International Symposium on Software Testing and Analysis*, pages 146–157. ACM, 2019. 3
- [47] Xiaofei Xie, Lei Ma, Haijun Wang, Yuekang Li, Yang Liu, and Xiaohong Li. Diffchaser: Detecting disagreements for deep neural networks. In *Proceedings of the Twenty-Eighth International Joint Conference on Artificial Intelligence, IJCAI-19*, pages 5772–5778. International Joint Conferences on Artificial Intelligence Organization, 7 2019. 4
- [48] Guoming Zhang, Chen Yan, Xiaoyu Ji, Tianchen Zhang, Taimin Zhang, and Wenyuan Xu. Dolphinattack: Inaudible voice commands. In *Proceedings of the 2017 ACM SIGSAC Conference on Computer and Communications Security*, pages 103–117. ACM, 2017. 1
- [49] Jie Zhang, Mark Harman, Lei Ma, and Yang Liu. Machine learning testing: Survey, landscapes and horizons. *IEEE Transactions on Software Engineering*, 2019. 3

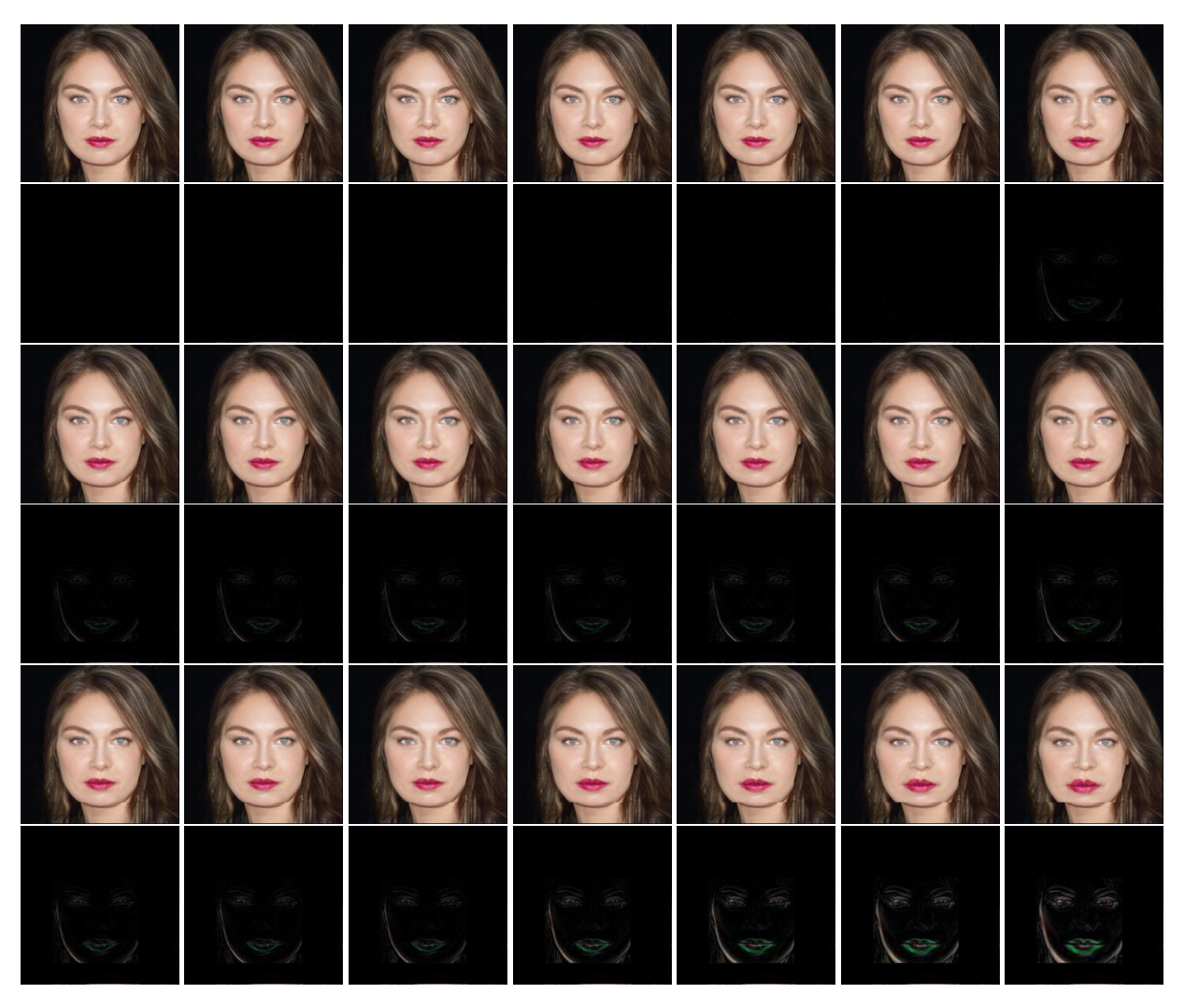


Figure 9: Original facial image ( ID in *CelebA* is 000737 ) and morphed facial images with proprietary morphing field measured by  $\ell_2$ -norm. The first image is the original facial image and the following 20 images are morphed with proprietary morphing fields while images in black background are difference images of original facial image and morphed facial image. The  $\ell_2$ -norm values are  $\{2,4,6,8,10,100,110,120,130,140,150,160,170,180,190,200,300,400,500,600\}$ .

## A. Appendix

In this section, we present some high-resolution visualization of our original faces and morphed facial images with different intensity of proprietary morphing fields measured by  $\ell_2$ -norm,  $\ell_{\infty}$ -norm and multiplier  $\delta$ , and their difference images.

Figure 9 - Figure 13 present us the original facial image and morphed facial images with learned proprietary morphing fields measured by  $\ell_2$  norm. The  $\ell_2$ -norm value is set to  $\{2,4,6,8,10,100,110,120,130,140,150,160,170,180,190,200,300,400,500,600\}$ . Figure 14 - Figure 18 present us the original facial image and morphed facial images with learned proprietary morphing fields measured by  $\ell_\infty$  norm. The  $\ell_\infty$ -norm value is set to  $\{0.1,0.2,0.3,0.4,0.5,1.0,1.1,1.2,1.3,1.4,1.5,1.6,1.7,1.8,1.9,2.0,3.0,4.0,5.0,6.0\}$ . Figure 19 - Figure 23 present us the original facial image and morphed facial images with learned proprietary morphing fields enhanced by multiplier  $\delta$ . The multiplier  $\delta$  is set to  $\{0.2,0.4,0.6,0.8,1.0,1.2,1.4\}$ .

These figures demonstrated that these high-resolution images revealed that our morphed facial images with proprietary morphing fields still maintain a well-performed visual quality when the intensity of proprietary morphing fields increased.

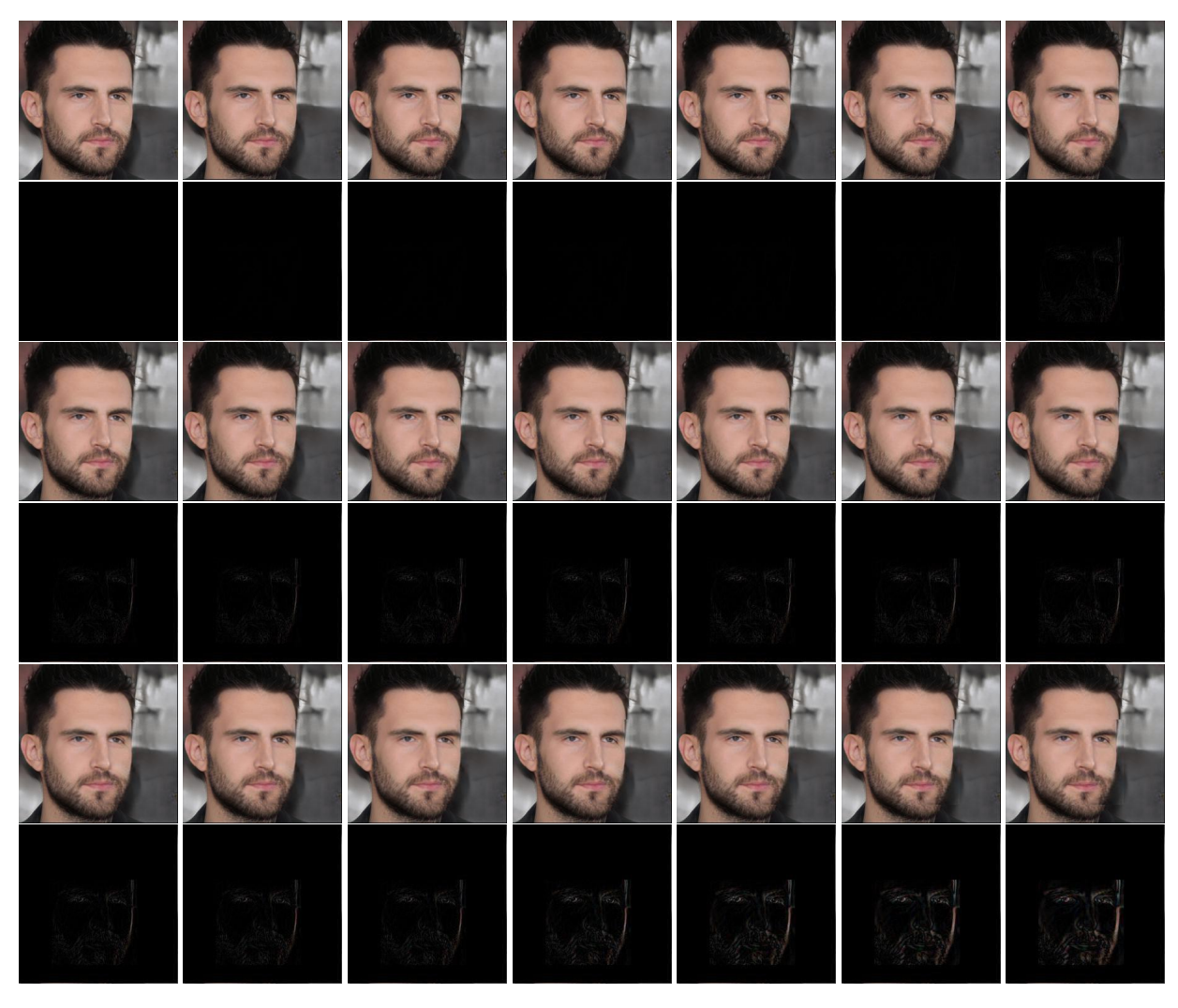


Figure 10: Original facial image ( ID in CelebA is 003668 ) and morphed facial images with proprietary morphing field measured by  $\ell_2$ -norm. The first image is the original facial image and the next 20 images are morphed with proprietary morphing fields while images in black background are difference images of original facial image and morphed facial image. The  $\ell_2$ -norm values are  $\{2,4,6,8,10,100,110,120,130,140,150,160,170,180,190,200,300,400,500,600\}$ .

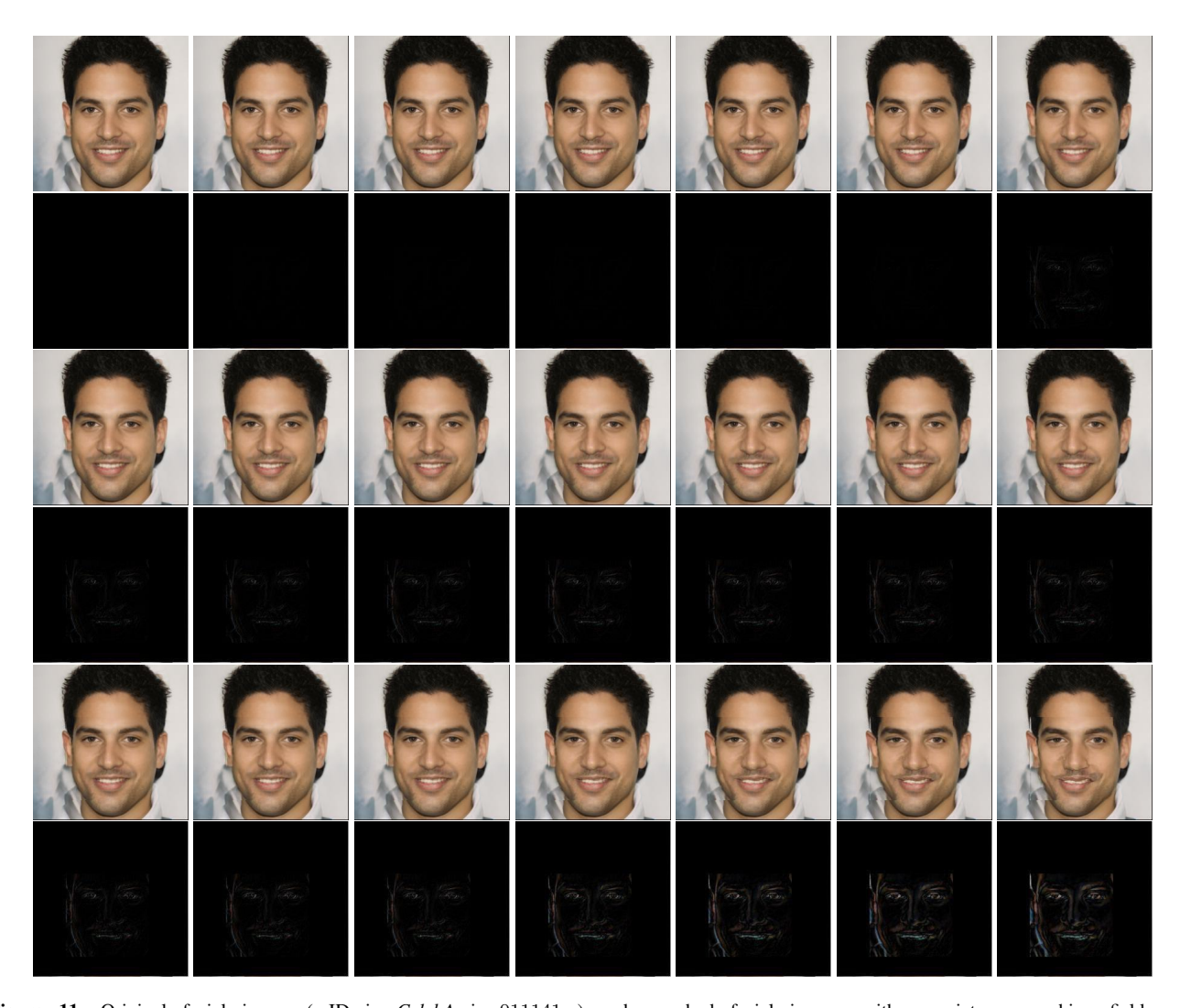


Figure 11: Original facial image ( ID in CelebA is 011141 ) and morphed facial images with proprietary morphing field measured by  $\ell_2$ -norm. The first image is the original facial image and the next 20 images are morphed with proprietary morphing fields while images in black background are difference images of original facial image and morphed facial image. The  $\ell_2$ -norm values are  $\{2,4,6,8,10,100,110,120,130,140,150,160,170,180,190,200,300,400,500,600\}$ .

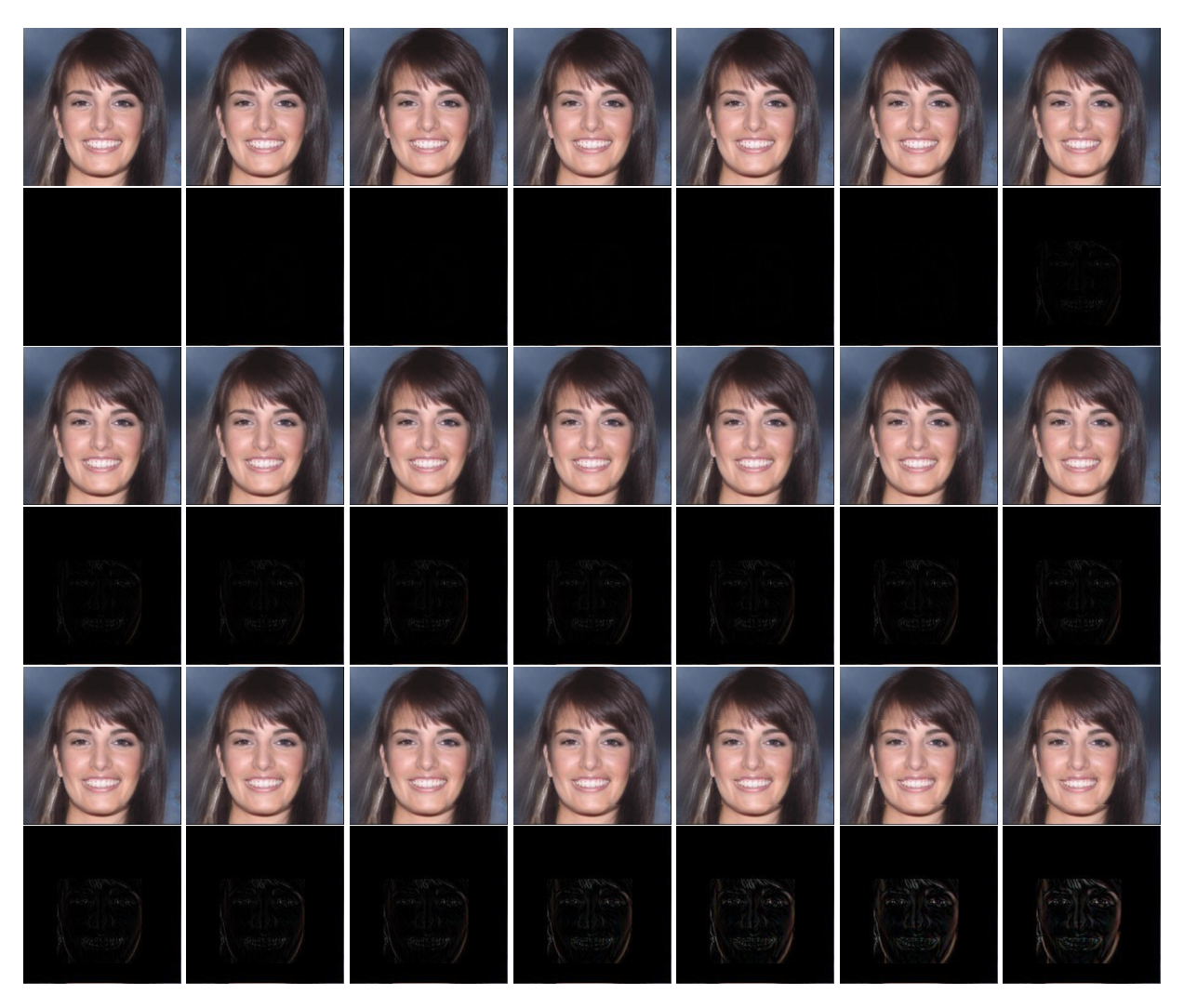


Figure 12: Original facial image ( ID in CelebA is 011910 ) and morphed facial images with proprietary morphing field measured by  $\ell_2$ -norm. The first image is the original facial image and the next 20 images are morphed with proprietary morphing fields while images in black background are difference images of original facial image and morphed facial image. The  $\ell_2$ -norm values are  $\{2,4,6,8,10,100,110,120,130,140,150,160,170,180,190,200,300,400,500,600\}$ .



Figure 13: Original facial image ( ID in CelebA is 016353 ) and morphed facial images with proprietary morphing field measured by  $\ell_2$ -norm. The first image is the original facial image and the next 20 images are morphed with proprietary morphing fields while images in black background are difference images of original facial image and morphed facial image. The  $\ell_2$ -norm values are  $\{2,4,6,8,10,100,110,120,130,140,150,160,170,180,190,200,300,400,500,600\}$ .

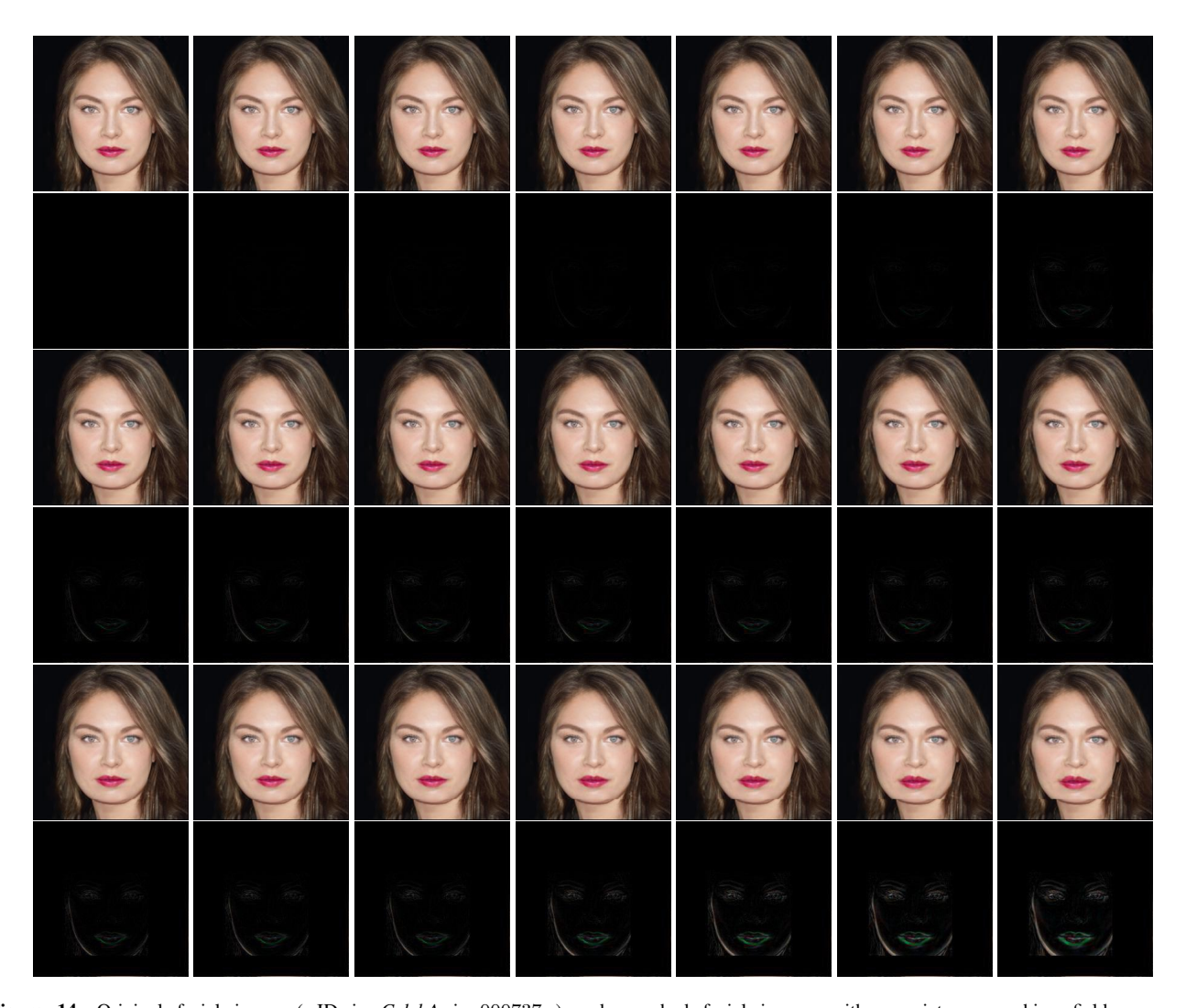


Figure 14: Original facial image ( ID in CelebA is 000737 ) and morphed facial images with proprietary morphing field measured by  $\ell_{\infty}$ -norm. The first image is the original facial image and the following 20 images are morphed with proprietary morphing fields while images in black background are difference images of original facial image and morphed facial image. The  $\ell_{\infty}$ -norm values are  $\{0.1, 0.2, 0.3, 0.4, 0.5, 1.0, 1.1, 1.2, 1.3, 1.4, 1.5, 1.6, 1.7, 1.8, 1.9, 2.0, 3.0, 4.0, 5.0, 6.0\}$ .

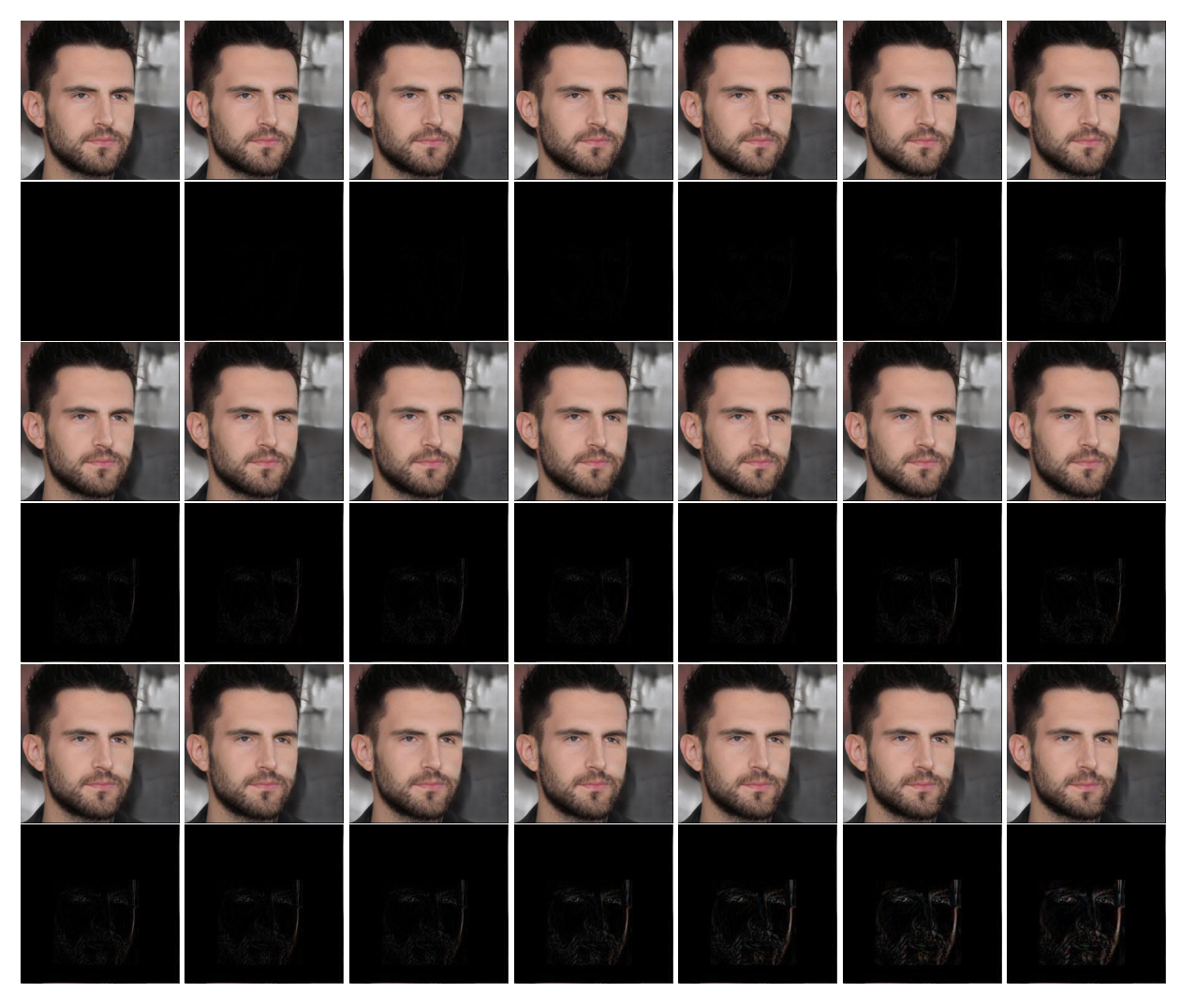


Figure 15: Original facial image ( ID in *CelebA* is 003668 ) and morphed facial images with proprietary morphing field measured by  $\ell_{\infty}$ -norm. The first image is the original facial image and the next 20 images are morphed with proprietary morphing fields while images in black background are difference images of original facial image and morphed facial image. The  $\ell_{\infty}$ -norm values are  $\{0.1, 0.2, 0.3, 0.4, 0.5, 1.0, 1.1, 1.2, 1.3, 1.4, 1.5, 1.6, 1.7, 1.8, 1.9, 2.0, 3.0, 4.0, 5.0, 6.0\}$ .

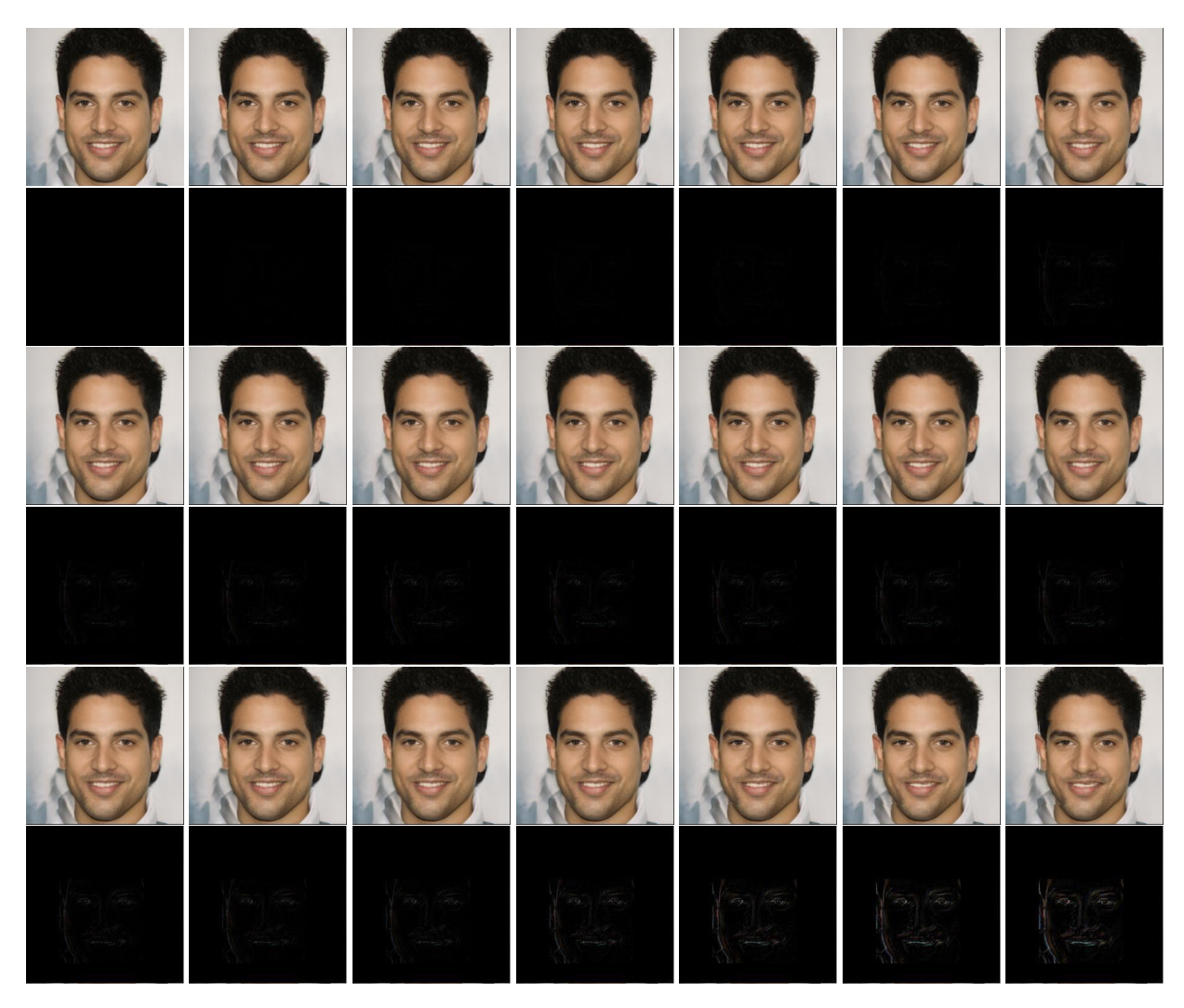


Figure 16: Original facial image ( ID in *CelebA* is 011141 ) and morphed facial images with proprietary morphing field measured by  $\ell_{\infty}$ -norm. The first image is the original facial image and the next 20 images are morphed with proprietary morphing fields while images in black background are difference images of original facial image and morphed facial image. The  $\ell_{\infty}$ -norm values are  $\{0.1, 0.2, 0.3, 0.4, 0.5, 1.0, 1.1, 1.2, 1.3, 1.4, 1.5, 1.6, 1.7, 1.8, 1.9, 2.0, 3.0, 4.0, 5.0, 6.0\}$ .



Figure 17: Original facial image ( ID in *CelebA* is 011910 ) and morphed facial images with proprietary morphing field measured by  $\ell_{\infty}$ -norm. The first image is the original facial image and the next 20 images are morphed with proprietary morphing fields while images in black background are difference images of original facial image and morphed facial image. The  $\ell_{\infty}$ -norm values are  $\{0.1, 0.2, 0.3, 0.4, 0.5, 1.0, 1.1, 1.2, 1.3, 1.4, 1.5, 1.6, 1.7, 1.8, 1.9, 2.0, 3.0, 4.0, 5.0, 6.0\}$ .



Figure 18: Original facial image ( ID in *CelebA* is 016353 ) and morphed facial images with proprietary morphing field measured by  $\ell_{\infty}$ -norm. The first image is the original facial image and the next 20 images are morphed with proprietary morphing fields while images in black background are difference images of original facial image and morphed facial image. The  $\ell_{\infty}$ -norm values are  $\{0.1, 0.2, 0.3, 0.4, 0.5, 1.0, 1.1, 1.2, 1.3, 1.4, 1.5, 1.6, 1.7, 1.8, 1.9, 2.0, 3.0, 4.0, 5.0, 6.0\}$ .



Figure 19: Original facial image ( ID in *CelebA* is 000737 ) and morphed facial images with proprietary morphing field enhanced by multiplier  $\delta$ . The first image is the original facial image and the following 7 images are morphed with proprietary morphing fields while the second row is difference images of original facial image and morphed facial image. The  $\delta$  values are  $\{0.2, 0.4, 0.6, 0.8, 1.0, 1.2, 1.4\}$ .



Figure 20: Original facial image ( ID in *CelebA* is 003668 ) and morphed facial images with proprietary morphing field enhanced by multiplier  $\delta$ . The first image is the original facial image and the next 7 images are morphed with proprietary morphing fields while the second row is difference images of original facial image and morphed facial image. The  $\delta$  values are  $\{0.2, 0.4, 0.6, 0.8, 1.0, 1.2, 1.4\}$ .

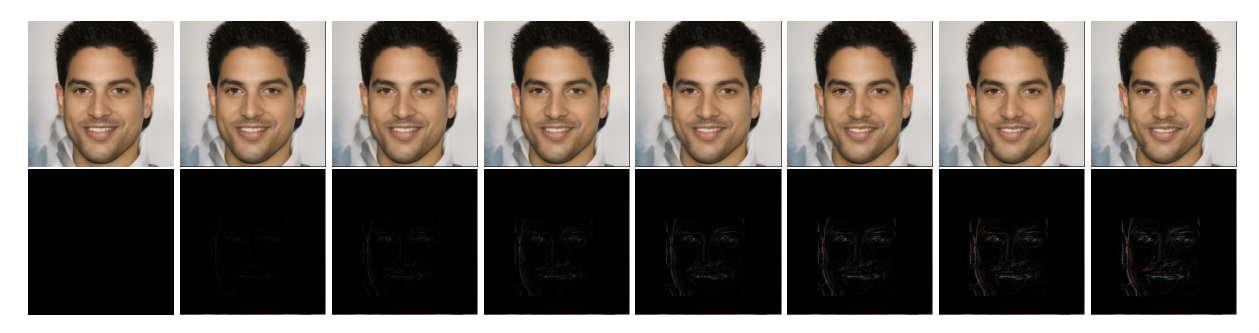


Figure 21: Original facial image ( ID in *CelebA* is 011141 ) and morphed facial images with proprietary morphing field enhanced by multiplier  $\delta$ . The first image is the original facial image and the next 7 images are morphed with proprietary morphing fields while the second row is difference images of original facial image and morphed facial image. The  $\delta$  values are  $\{0.2, 0.4, 0.6, 0.8, 1.0, 1.2, 1.4\}$ .



Figure 22: Original facial image ( ID in CelebA is 011910 ) and morphed facial images with proprietary morphing field enhanced by multiplier  $\delta$ . The first image is the original facial image and the next 7 images are morphed with proprietary morphing fields while the second row is difference images of original facial image and morphed facial image. The  $\delta$  values are  $\{0.2, 0.4, 0.6, 0.8, 1.0, 1.2, 1.4\}$ .



Figure 23: Original facial image ( ID in *CelebA* is 016353 ) and morphed facial images with proprietary morphing field enhanced by multiplier  $\delta$ . The first image is the original facial image and the next 7 images are morphed with proprietary morphing fields while the second row is difference images of original facial image and morphed facial image. The  $\delta$  values are  $\{0.2, 0.4, 0.6, 0.8, 1.0, 1.2, 1.4\}$ .